Dual-Parameter Opto-Mechanical Fiber Optic Sensors for Harsh Environment Sensing: Design, Packaging, Calibration, and Applications

by

Tian You Richard Liang

A thesis
presented to the University of Waterloo
in fulfillment of the
thesis requirement for the degree of
Master of Applied Science
in
Mechanical Engineering

Waterloo, Ontario, Canada, 2014

Author's Declaration

I hereby declare that I am the sole author of this thesis. This is a true copy of the thesis, including any required final revisions, as accepted by my examiners.

I understand that my thesis may be made electronically available to the public.

Abstract

This thesis concerns with the development of a dual-parameter sensor based on fiber Bragg grating (FBG) and a packaging design for high pressure sensing in harsh environment.

This thesis starts by introducing a novel design of a partially coated FBG, using a metallic insert and a thermal curing epoxy. An analytical opto-mechanical model, based on couple mode theory, was developed and presented. The experimental and modelling result of the optical response of the partially coated FBG were compared and shown to be in excellent agreement. The experiments were executed on a custom-built fiber optic calibration station. The coated FBG sensor has a temperature sensitivity of $26.9 \pm 0.3\, pm/°C$, which is 2.7 times higher than a bare fiber; and a force sensitivity of $0.104\, nm/N$, which is 13 times smaller than a bare fiber. The zero reference of the sensor has a drift of a maximum of 70 pm but the sensor is shown to settle within $\pm 5\, pm$ after 3 thermal cycles and 10 tensile loading cycles.

A low profile packaging design is presented for a maximum pressure of 20.68 MPa (3000 psi) for harsh environment applications. A detailed study with FEM analysis revealed the optimal design for the package's sleeve thickness is 0.5 mm. The temperature sensitivity is in close agreement with the unpackaged coated sensor with 10% difference. Compared to the modelling, the equivalent force sensitivity is 27% lower due to prototype dimensional uncertainties and modelling uncertainties with the material properties. The lack of pre-tension of the FBG sensor in the package also attributed to lower force sensitivity at pressure level lower than 4.13 MPa (600 psi).

Acknowledgements

I would like to express my gratitude to my supervisor, Professor Ehsan Toyserkani, for his support, advice, and encouragement in the past two years. I also would like to thank Dr. Hamid Alemohammad for his valuable advice and guidance on opto-mechanical modelling which has significantly helped enhance my knowledge in the field of optics. I hereby express my gratitude to my thesis reviewing committee members, Professor Adrian Gerlich and Professor Soo Jeon for their review, comments and suggestions.

I am pleased to acknowledge the financial support from Government of Ontario for Queen Elizabeth II Graduate Scholarships in Science and Technology.

I would like to thank my colleagues at the Mutli-Scale Additive Manufacturing lab at University of Waterloo - Dr. Mihaela Vlasea and Amir Azhari for their motivational support, as well as Farid Behzardian, Esmat Sheydaeyan, Mark Park, Xixi Zhang, Steven Tong, Oliver Jay, Evan Wheat, Daniel Pradon, Elahe Jabari, Ahmad Basalah, Bahareh Marzban for their help and encouragement.

I would also like to take the opportunity to thank my dearest friends from my undergraduate Mechatronics Engineering program: Sirui Song, Eugene Li, Dorothy Lui, Richard Chang, for giving me a supportive environment both in personal and academic related matters. In addition, I would like to thank Sibi Sutty, Jeff Luo, Wayne Hsu, Trevor Choi, Sally Ip, Max Huang, Sean Li, and Mohamed Oudah for the memorable and precious friendship during my graduate program. It simply would not have been the same without my friends' support.

Lastly I would like to express my deepest gratitude to family, particularly to my mother – Suyue, her boyfriend - David Liao, my sister - Christy, and my grandparents for their continued support and motivation.

In loving memory of my maternal grandfather,

who taught me how to learn.

Table of Contents

List of Figures

List of Tables

List of Abbreviations

ID – Inner Diameter

OD – Outer Diameter

FBG – fiber Bragg grating

CTE - Coefficient of Thermal Expansion

DAQ - Data AcQuisition system

FEM - Finite Element Model

Nomenclature

Symbol	Description
n_{eff}	Effective refractive index
n_{core}	Effective refractive index of fiber core
$n_{cladding}$	Effective refractive index of cladding
δ	Detuning function
ϕ	Grating chirp
κ	"AC" coupling coefficient
$\widehat{\sigma}$	"DC" coupling coefficient
v_f	Fringe visibility
β	Launch angle
$\overline{\delta n_{eff}}$	Average refractive index change
p_{ij}	Element of Pockel's constant matrix
ϵ_i	Element of strain tensor in i principal axis
$\partial n/\partial T$	Change in refractive index to temperature change
L_G	Effective length of FBG
λ_B	Nominal Bragg wavelength at reference temperature
Λ_G	Grating pitch
α_f	Coefficient of thermal expansion of fiber (silica)
R	Forward propagating mode intensity function
S	Backward propagating mode intensity function
ρ	Forward to backward mode amplitude ratio
$r(\lambda)$	Reflectivity as a function of the wavelength
R^2	Coefficient of determination
ΔT	Change in temperature
ΔP	Change in pressure
ΔF	Change in force
$\Delta\epsilon$	Change in strain in the axial direction
$\Delta Peak\ 1$	Wavelength shift of Bragg wavelength 1
$\Delta Peak\ 2$	Wavelength shift of Bragg wavelength 2

1 Introduction

Fiber optic has its first root in the application of biomedical industry for use as flexible endoscopes in the first half of twentieth century. The modern application of fiber optic was enabled by the development of low-loss optical fibers in the 1970s. Fiber optic technology has since revolutionized the telecommunication industry and has played a pivotal role in the revolution of the Information Age. The ability to communicate large amount of information in the optical medium has made fiber optic a much better contender in comparison with the conventional copper based electrical transmission. Also, fiber optic has the added benefit of high reliability, low signal distortion, and low loss over long distances.

Exploiting the fiber optic's exceptional capability of immunity to electromagnetic interferences, there is a staggering opportunity to fill the demand of optical based environment sensors. With the continuous development of fiber materials and packaging strategies, optical fibers have not just taken the role in the field of digital communication, but also have rooted itself as an ideal platform for interdisciplinary and multifunctional integration for sensing applications.

Fiber optic's ability to multiplexing in a serial fashion, reliable remote sensing, tunable sensitivity, miniaturization/low profile, electrically passive operation, immunity to electromagnetic interference (EMI), and self-referencing are deemed as the unique advantages of fiber optic based sensors over other existing sensors.

The development of fiber optic sensors has made the sensor available to a wide array of application areas such as oil and gas, nuclear, aerospace, power generation, biomedical, and water resources. Udd and Spillman [1] defined three distinctive waves of fiber optic sensor technology. The first wave of fiber optic development is fiber optic gyroscope and hydrophone, based on Sagnac effect and Mach-Zehnder interferometers, respectively. The second wave is based on Fabry-Perot interferometry. Last but not least is fiber Bragg

gratings (FBG). All three fiber optic sensor technologies, which are well documented in literature, have undergone significant research and proof of practicality in both military and commercial applications today.

FBG is an adopted technology for use in telecommunication industry. It has commercial applications in the areas such as optical filtering, dispersion compensation, laser stabilization, and erbium amplifier gain flattening [2]. FBGs also display excellent performance to in-situ temperature and mechanical strain perturbation. The sensing mechanism of FBG is based on variations of the refractive index and grating pitch under environment perturbations, particularly to temperature and applied mechanical strain. An FBG has a linear optical response to temperature and strain change due to thermo-optic and photo-elastic effects. Combined with the benefit of EMI immunity and electrically passive, an FBG can be integrated as an ideal solution for either temperature or strain measurement in harsh environments. Alternatively, FBG's sensitivity to other environment parameter, such as corrosion, moisture, acoustic, and vibration, can be exploited by coupling these parameters to temperature and strain on the fiber.

1.1 Challenges

The main challenges in the application of FBG arises from the sensitivity of the Bragg wavelength to both temperature and strain perturbation from the environment.

Some of the most popular technique for dual-parameter sensing requires the use of two separate FBG sensors in a cantilever or diaphragm structure. In this configuration, one FBG is placed to directly interact with both strain and temperature effects while another FBG is placed in vicinity as a temperature compensation sensor [3]–[7]. Two separate FBGs are required for this technique, which adds complexity into package design and the assembly process. Depending on the geometric design, this configuration can be prohibitive to implement multiplexing of multiple sensors in series. A way to circumvent the use of two separate FBGs is to inscribe dual FBG gratings onto the same location [8]. However, there is reported issue with the stability of the second Bragg

grating over long term use. It is also reported that the 2nd order diffraction as a result of grating inscription can be utilized as the temperature and strain sensitivity is wavelength dependent [9]. This method is promising but requires added optical spectrum analyzer to cover ranges from approximately 700nm to 1600nm, which adds cost and complexity to the optical interrogation configuration. Another promising technique, proposed by James et al., splices two of the same FBGs with different cladding diameters right next to each other [10]. Since FBGs have the same temperature sensitivity but different strain sensitivity due to difference in diameter. The difficulty in alignment of the FBGs with different cladding size, as well as the degraded mechanical strength of the fiber after the splice, poses challenges for practical implementation of this technique.

Following the same approach, it is understood that the dual parameter sensing capability if different parts of the FBGs have different sensitivity to temperature and strain. A popular technique is to apply a layer of coating on the FBG with different coefficient of thermal expansion. Standard type I FBG have degradation temperature starting at 300°C [11]. To avoid causing permanent damage, many low temperature metal coating techniques are proposed in the literature using methods such as sputtering, electroplating, electroless plating, vacuum brazing, vapour deposition, electrowinning [12]–[15]. However, these processes suffer from the need of precise control of process parameters, the need for bilayer coating, limitation for patterning, high cost, and accessibility for mass production.

For harsh environment sensing, there is also existing challenges to package and protect the FBG for reliable operation. The presence of hydrogen-rich and other foreign chemical agents in the environment can increase growth of the flaws on FBG surface which can lead to premature failure [16]. To achieve a high sensor count for distributed sensing using Wavelength Division Multiplexing (WDM), the amount of strain imposed on the fiber must also be optimized to accommodate a cost-effective number of sensors to be integrated onto the same fiber optic cable. According to the report by Smart Fibres

[17], the oil and gas industry is facing difficulty in measuring pressure in multi-zone oil wells, difficulty in distributed pressure measurement, and difficulty in sensing in high pressure or high temperature wells. A number of patents application and literature paper have attempted to address the issue of packaging with metal alloy tube, bourdon tube, and capillary tubes [4], [5], [18]. These strategies have the merit of an extremely robust design; but they have the added complexity as multiple FBGs are still required for temperature and strain discrimination. In addition, these designs require a large footprint that adds cost and hinders the deployment of such sensors in harsh environments.

1.2 Purpose and Motivation

FBG has the advantage of small size, distributed sensing, electrically passive, immunity to electromagnetic interference, and low loss over long distances. These advantages make the FBG sensor an ideal solution to be used in harsh environment sensing for application area such a nuclear plants, high temperature furnaces, jet engine, and oil and gas.

The purpose of this thesis is to propose a novel FBG coating and packaging design for the application for high pressure down-hole oil well monitoring. The goal of the coating is to provide a simple, easy to assemble, and economical technique to enable the simultaneous measurement of temperature and strain without sacrificing measurement accuracy. The performance of this design is rigorously tested and reported for validation. The package design aims to protect the coated fiber and optimize the imposed strain while miniaturizing the entire package within a ¼" stainless steel pipe.

The application of such packaged FBG sensor is particularly useful in the oil and gas industry. There is a demonstrated need for high accuracy pressure sensing for the monitoring of the oil well reservoir condition. With the information of multi-zone pressure and temperature measurement, production engineers can assess well condition better to mitigate the risk of early equipment failure. Engineers can also use the

information to better optimize the well production performance by enhanced zonal control in the well [17]. In addition to wells, the applications in the oil and gas pipelines monitoring can also be benefited. Over time, many of the existing pipelines are at risk of gas and liquid leakage from degradation due to Stress Corrosion Cracking (SCC) and wall thinning.

1.2.1 Market Segmentation

In recent years, the cost of key optical components has fallen drastically as the mass production techniques for optoelectronic devices mature. This has driven the standard and quality of telecommunication industry using fiber optic technology to increase substantially. A similar impact is made on the quality of fiber optic sensors. The increased in reliability has gained substantial traction in the market acceptance of the fiber optic sensor technology. According to "BCC Research" in 2011, the global fiber optic market value is expected to reach $2.5 billion in 2017 with a compound annual growth rate of 10.5% [19]. In a separate market research report by "Frost and Sullivan", the world's fiber optic sensor market alone is expect to reach $3.31 billion in 2017 [20]. A large portion of the fiber optic sensor market is adopted by the oil and gas industry, as the industry is known to have a record of abundance of investment funding [21]. The "Photonic Sensor Consortium Survey" by IGI Group estimates that a large 73% of the total fiber optic sensor market will be distributed fiber optic sensor in the oil and gas industry [22]. This market size is expected to reach $1.1 billion in 2017.

1.3 Thesis Objectives and Contributions

The objective statement of this thesis is:

Design and Characterization of a Dual-Parameter Opto-Mechanical Fiber Optic Sensors for Harsh Environment Sensing

---

To this end, the following tasks were pursued,

1. Designed and implemented a fiber partial coating strategy using a metallic insert and thermal curing epoxy,
2. Adopted, simulated, and validated an opto-mechanical model based on couple mode theory,
3. Characterized the performance of the dual-parameter FBG sensor in the lab,
4. Investigated stability and repeatability of the FBG sensor,
5. Designed, modelled, and characterized a package design for high pressure sensing applications.

1.4 Thesis Outline

This thesis has eight chapters. Chapter 1 focuses on the applications of FBG sensor and outlines the current challenges in dual parameter sensing as well as package design. Also, the market need and opportunity for dual parameter sensing in harsh environment is discussed. Chapter 2 reviews the fundamentals of FBG with a literature review of the techniques for dual parameter sensing, on-fiber modulation, and packaging for harsh environment. The design of a half-coated FBG sensor is proposed and implemented using a thermal curing epoxy as the bonding agent in Chapter 3. The experiment setup, data collection and processing procedure are also discussed. Couple mode theory and opto-mechanical modelling is introduced and validated in Chapter 4. Chapter 5 presents the investigation of the half-covered FBG sensor. Sensor dynamics, characteristics and repeatability performance are examined. The design of a mechanical package for high pressure harsh environment sensing is proposed, optimized, implemented, and analyzed in Chapter 6. Chapter 7 concludes the findings from this thesis and Chapter 8 outlines the recommendations of future work.

2 Background/Literature Review

In this chapter, an overview of the fundamentals of the fiber optic, fiber gratings structure, types and modulation will be discussed. The chapter is followed by a literature review on the techniques of dual-parameter discrimination, mechanical modulation of fiber optics, and current strategies for harsh environment sensing.

2.1 Fiber Optic Structure and Gratings

A fiber optic cable is a cylindrical filament made of two layer of silica (SiO_2) with slightly different refractive index. To enhance the mechanical strength, the fiber optic cable is also packaged with a polymeric jacket as shown in Figure 2-1a. The center region of the fiber optic is called the core while the immediate layer outside of it is called the cladding. Light traveling inside the core of the fiber optic cable can be confined by total internal reflection. This occurs by designing a slightly higher refractive index in the core than the cladding [2], usually by doping the core with Germanium, as seen in Figure 2-1b. The condition for total internal reflection also requires that the launch angle (β) of the light entering the fiber should satisfy,

$$\beta < arcsin\sqrt{n_{core}^2 - n_{cladding}^2} \tag{2.1}$$

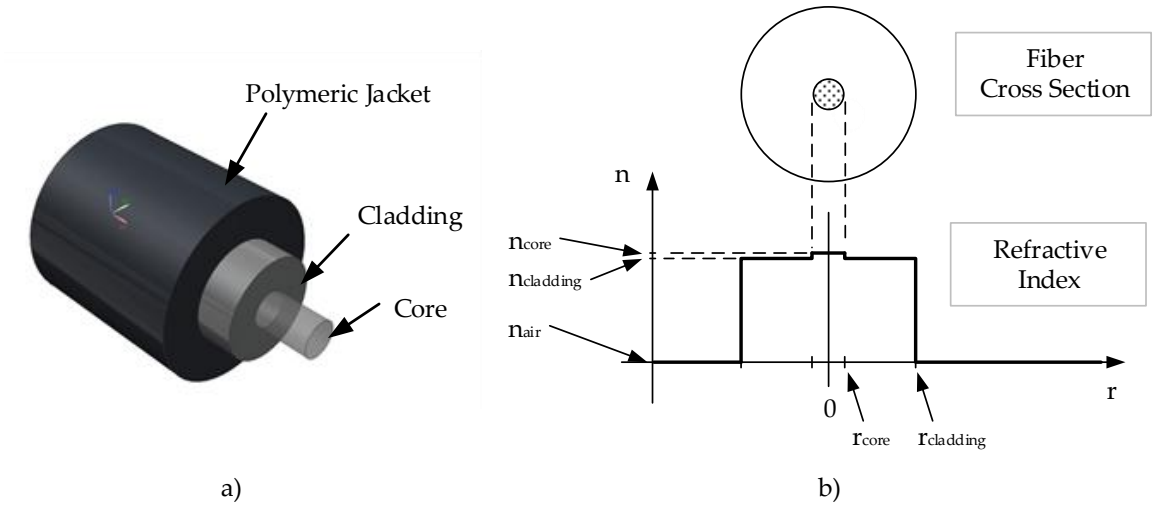

Figure 2-1 a) Fiber optic structure b) refractive index profile.

where the term $\sqrt{n_{core}^2 - n_{cladding}^2}$ is also called the numerical aperture NA, which is used to characterize the refractive index in a fiber optic cable. A standard Corning© SMF-28© single-mode fiber optic cable, commonly used for telecommunication applications, has a diameter of 8.2 μm and 125 μm for core and cladding, respectively, with a numerical aperture of 0.14 [23].

Fiber grating can be produced by inducing a periodic and permanent modulation of refractive index on the fiber optic cable. Fiber gratings are generalized into two categories - Long Period Grating (LPG) and Fiber Bragg Grating (FBG).

Long Period Grating, also called transmission grating, has a grating pitch in the order of millimetres. LPG requires less complexity to manufacture due to its larger grating spacing. LPG couples the fundamental mode and the cladding mode of the propagating light. The coupling causes the absorption of specific wavelengths, which can be measured in the transmission spectra.

Fiber Bragg Grating, consist of gratings with much shorter grating pitch, which is in the same order of magnitude as the wavelength of the propagating light. The fundamental difference between a LPG and FBG is that FBG reflects a specific band of wavelength of the passing electromagnetic wave while LPG absorbs it.

The operating principle of FBG is based on the Bragg Law, established by Sir William Lawrence Bragg in 1915, which formulated how X-Rays can be diffracted from crystals. The resonant condition, also called the Bragg condition, defines the reflected wavelength of light (λ_B) as a function of the effective refractive index (n_{eff}) of the traveling medium (waveguide) and the spacing between the gratings (Λ_G),

$$\lambda_B = 2n_{eff}\Lambda_G \tag{2.2}$$

If a broadband spectrum of electromagnetic wave is incident on the FBG, the band of the spectrum that matches closely with the Bragg wavelength will undergo strong reflection. The reflection is caused by the resonance conditions coupling between the forward and

backward propagating modes of the incident electromagnetic wave [24]. The range of spectrum being reflected, or the bandwidth of the Bragg wavelength, is a function of the total number of gratings (N) and the strength of index modulation (S) in the core.

The photosensitivity of germanium doped silica fiber was first observed by K.O. Hill et al. at the Canadian Communication Research Centre in 1978 [25]. Germanium is the commonly chosen element doped in the core region of the silica fiber to increase its refractive index. There exists imperfections within the silica glass structure as the doped Germanium forms defect bonds with neighboring oxygen and silicon atoms, forming Germanium Oxide (GeO_n) or Germanium-Silicon (Ge-Si) bonds. When exposed to external radiation, it was found that the core refractive index can be further increased by breaking these defect bonds [24]. Hence, the performance of the fiber waveguide can be tuned by periodically exposing the fiber to radiation. This creates a periodic modulation of refractive index, which ultimately affects the optical pass band performance if the grating pitch satisfies (2.2).

2.2 Grating Modulation

FBGs can be categorized into four classes as described below.

Common: periodic grating pitch of refractive index along the fiber is consistent and the grating planes are perpendicular to the longitudinal axis of fiber

Chirped: periodic grating pitch of refractive index along the fiber increase/decrease monotonically. The grating planes are perpendicular to the longitudinal axis of fiber

Blazed: The grating planes are tilted at an angle to the longitudinal axis of the fiber

Apodized: the magnitude of the refractive index change follows an apodization function along the length of the grating

The FBG used for experiments in this thesis is an apodized one.

2.3 Types of FBGs

Besides the different classes of grating modulation for FBG, FBGs can be generalized into several types, based on the manufacturing processes and the grating characteristics. The following sections review the five common classes of FBGs found in literature.

2.3.1 Type I Grating

Type I grating is the most common type of grating for commercial applications to date. It is manufactured by UV photon absorption process [26]. This process causes defect formation in a germanium doped silica core and densification of the glass matrix which ultimately results in refractive index change [27]. In this type of grating, the refractive index correlates positively with temperature change. However, at elevated temperature, the grating would start to degrade and the degradation could be characterized by the power law [28] [29]. The decay occurs due to thermal depopulation of trapped excited states, which reverts the gratings initially formed by UV exposure. Carriers absorb enough energy to escape and thus return to ground state. For reliable operation, Type I grating should not be subjected to temperature over 300 °C [11].

2.3.2 Type II

Type II grating is produced with a high peak power pulsed UV laser source. Due to the high power laser, the grating is formed through an induced damage in bulk optics [30]. This type of grating tends to exhibit high reflectivity (<99%) and is shown stable at temperature over 1000°C. However, it was also reported that the large damage in bulk optic also reduce the reliability and mechanical strength of the fiber [31].

2.3.3 Type In or IIA

Type In grating is fabricated similar to Type I but the UV exposure is written to highly stressed Ge-doped fiber. The continued exposure of the grating results in a secondary grating growth which finally results in a decrease in refractive index [11]. The reflectivity was reported to drop below 90% at temperature above 550°C [32]. With

optimized manufacturing process, Type In grating was shown to have a maximum stable operating temperature up to 700 °C [33].

2.3.4 Regenerated Gratings

This type of grating, sometimes also called Chemical Composition Grating, is another optimization of the standard Type I grating. The manufacturing process involves an extra step, called hydrogen loading, which exposes the optical fiber to hydrogen gas prior to UV inscription. The exposure to high-pressure hydrogen gas saturates the fiber's glass matrix with hydrogen. Subsequent UV inscription on the fiber results in additional Si-OH or Ge-OH bond, which further increases the refractive index at the grating location compared to the standard Type I grating. The FBG then undergoes an annealing process at 600-700°C. The hydroxyl group diffuses and forms water molecules within the glass matrix [34]. Canning reported that regenerated grating possesses high stability for temperature above 1000°C [35].

2.3.5 Femtosecond Pulse Duration Infrared Laser Induced Gratings

Large index change in bulk glass can be induced by using ultra high peak power in femtosecond pulse duration with an infrared laser system. The radiation causes non-linear multi-photon absorption/ionization process. The process causes dielectric breakdown in the fiber core, which results in localized melting, material compaction, and void formation. Nanosecond pulses ensure quality of the spectral performance as the irradiated zone is localized and the defect does not propagate. The induced defect had been shown to remain stable until the glass transition temperature of silica [36]. These type of grating has the advantage of withstanding extremely high temperature and remain stable up to 1000°C for silica based fiber [36] and >1750°C for sapphire based waveguides [37].

2.4 Discrimination of Temperature and Strain

The ability discriminate the effect of temperature and strain in FBG is an extremely important research topic. The benefits of accurately discriminating temperature and strain effect in an FBG are twofold [38]:

- Reduction of sensor complexity, size and cost
- Resolves issue with cross sensitivity

This topic has undergone intense research interest ever since the first discrimination method discussed and demonstrated by Xu et al. in 1994 [8]. This section explores the popular multi-parameter discrimination techniques documented in literature.

The simplest technique in dual parameter discrimination is to use two separate FBGs. Since it was technologically difficult to completely isolate the effect of temperature on one of the FBGs, the configuration involved the first FBG to be exposed to both mechanical load and temperature, while the second FBG was exposed to temperature only. The second FBG acted as a reference temperature measurement. Since both of these FBGs are under the exact same temperature perturbation and shared the same sensitivity to temperature variation, the effect of the strain loading could be isolated by subtracting the response of the first FBG by the second one. Many arrangements of this dual FBG configuration had been proposed in the literature. Two types of the most common arrangement in practical application were serial deployment of FBGs or in the form of common-mode rejection.

Maron demonstrated a package design to utilize a pressure sensitivity structure that contains one fiber optic with two FBGs encapsulated in two isolated sections [3]. A diaphragm was used to convert pressure to strain one the first fiber. The second FBG was isolated from imposed strain and thus acts as the temperature compensation sensor. James et al. proposed a dual FBG setup where two FBGs, with different cladding size, are spliced next to each other [10], see Figure 2-2.

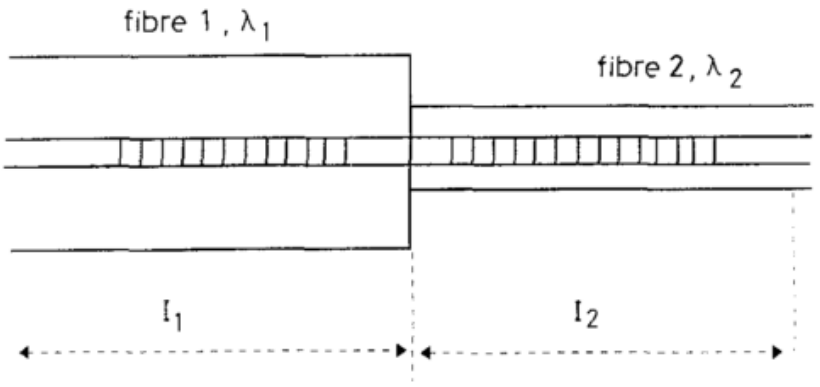

Figure 2-2 Spliced grating structure with different diameter [10].

The FBGs have the same grating pitch and therefore share the same temperature sensitivity but different strain sensitivity due to the difference in diameter. A resolution of ±17 με and ±1°C had been successfully obtained. In a similar serial fashion, Song et al. spliced two FBGs closely together within a capillary tube [5]. The first FBG was fixed at two ends by epoxy to the internal walls of the tube and acted as the temperature reference FBG. The second FBG was bonded only at one end. Hence when axial loading was applied, only the second FBG would respond to the strain. In another patented application, Maron and Kersey corroborated the feasibility to encapsulate an array of FBG sensors in a capillary tube for down-hole harsh environment multi-parameter sensing [4], as seen in Figure 2-3.

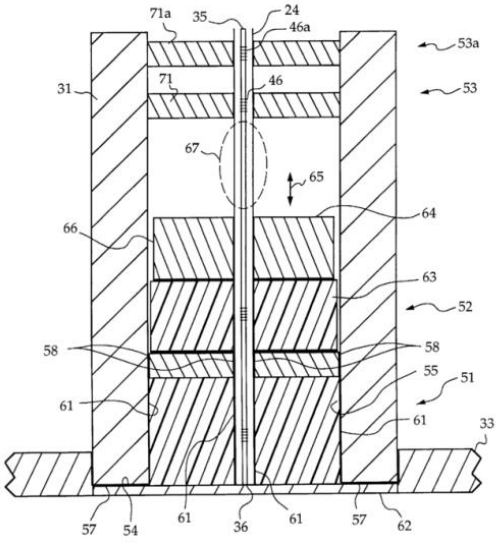

Figure 2-3 Encapsulated array of FBG sensors for harsh environment sensing [4].

The design composed of three separate FBGs, each used for temperature, pressure, and vibration sensing. The fiber was then terminated and bonded to the bottom of the capillary tube.

Alternatively, the arrangement relying on the use of diaphragm and cantilever beam had also gained a lot of research interest in literature. Birch et al. reported a sensor housing design having a flexible wall that was configured to deform in response to a pressure difference [6]. The first FBG was bonded on the flexible wall, which acted as a diaphragm as pressure differential between interior and exterior of the wall intensifies. The second FBG was bonded to a temperature reference body, located in proximity to the diaphragm. As shown in Figure 2-4, Yang et al. proposed a fairly involved mechanical design that integrates a two sided cantilever [7]. Two FBGs were bonded on the top and bottom of the cantilever beam. The technique of common mode rejection can be applied as temperature affects both of the FBGs to the same extent while change of external pressure deflects the cantilever, which finally caused opposing responses on the two FBGs.

Other than employing an extra FBG sensor to discriminate temperature and strain, many techniques were reported in literature to achieve in-situ discrimination of the two effects at the sensing point. One method was to inscribe a superposed double grating structures of different grating pitch, Λ_G. Xu et al. was the first to demonstrate this proof of concept in 1994 by inscribing two FBGs of Bragg wavelength of 850 nm and 1300 nm at the same location [8].

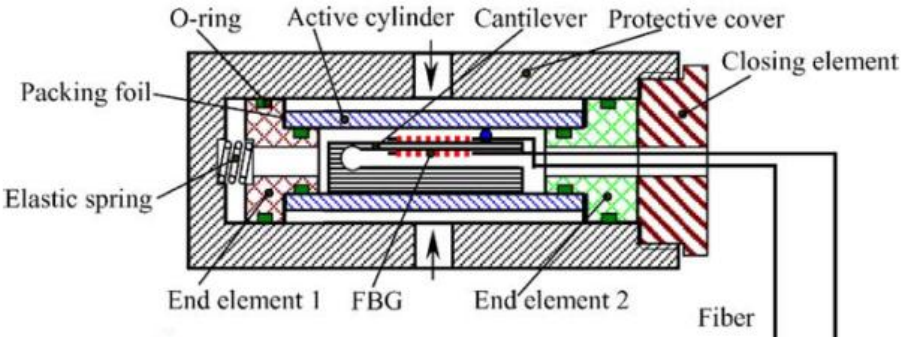

Figure 2-4 Temperature compensated high pressure package [7].

They showed that the photo-elastic and thermo-optic coefficients in the FBG are wavelength dependent. Therefore, the difference in sensitivity to strain and temperature at the two FBGs could be leveraged to solve and calibrate the sensor for simultaneous dual parameter measurement. Another similar optical technique was also proposed by observing the second-order diffraction wavelength of the inscribed FBGs. This technique was widely explored in literature. Brady et al. reported that the existence of 2nd order diffraction grating at integer multiples of the reflected peak frequency, given that the grating was inscribed using the interferometry technique [9]. The 2nd order peak has the property of a lower reflected power and this was accurately predicted by the respective Fournier coefficients. Echevarria and Quintela proposed an FBG with two observable peaks at 1535.85 nm and 767.94 nm. They have reported a sensitivity of 1.09 pm/$\mu\epsilon$ and 9.7 pm/°C for 1535.95 nm peak and 0.472 pm/$\mu\epsilon$ and 4.89 pm/°C [39].

Another optical technique was to use the birefringence of fiber optic to discriminate the effect of strain and temperature. In a polarization-maintaining (PM) fiber, the residual stress induced in the fiber cladding from the fiber draw process caused slightly different refractive index along the two mutually perpendicular axis (or polarization axes). Each perpendicular polarization of light, traveling in the waveguide, would separately response to the shear strain and the transverse strain. Kreger et al. demonstrated the package design with a side hole to fully utilize the PM fiber [40]. The design showed reasonable discrimination of temperature and pressure, with the pressure response being a second order function. Similar experimental result was demonstrated by using non circular fiber core geometry such as elliptical and bow-tie structure [41], [42].

2.5 On-Fiber Mechanical Modulation

The on-fiber modulation of FBG originated from the telecommunication requirement to use the FBG in applications such as spectral filter or dispersion compensation in an optical communication network. By coating the surface of an FBG with metallic thin film, the spectral response of the Bragg wavelength peak could be tuned by precisely controlling the strain or temperature perturbation.

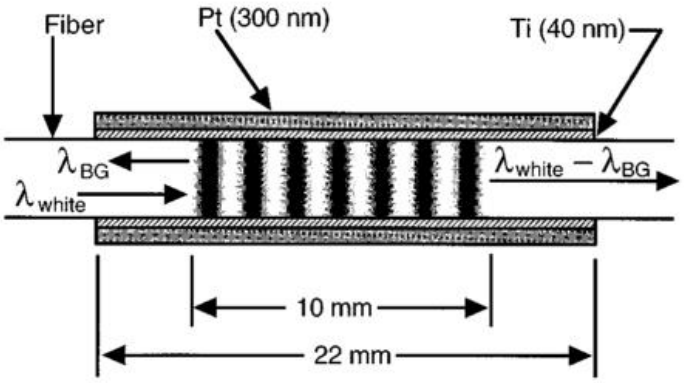

Figure 2-5 Structure of tunable FBG with coated bilayer [13].

The most popular technique to realize the precision control of Bragg wavelength was by the use of Joule heating on the thin film as documented in a variety of literature sources [13], [43]–[46].

The literature showed a growing research interest in the area of metal-coated optical fiber sensors. Typically, for the coating process of FBG, the coating consisted of a bilayer or multilayer configuration, with a different material for each layer, with an example shown in Figure 2-5. Since the FBG is made of silica, which is dielectric, the FBG requires a thin ($1 - 2\,\mu m$) and conductive layer for subsequent metal coating. Titanium was commonly used as this first layer [12], [13], [43]. By careful design of the material and thickness of the second layer to be deposited, the temperature sensitivity of the FBG could be tuned and optimized.

As discussed earlier, standard FBGs started to decay at temperature above 300°C [11]. Hence the metal coating process should never involve high temperature as to avoid damage to standard FBG. A literature review showed a number of lower temperature processes investigated – sputtering, electroplating, electroless plating, vacuum brazing, vapour deposition, electrowinning [12]–[15].

Li et al. studied methods to minimize residual stress in embedding FBG into metallic structures by the use of low temperature processes of magnetron sputtering and electroplating [12]. Enhanced adhesion was demonstrated using the configuration of $1\,\mu m$ titanium and $2\,\mu m$ nickel. Fox et al. also used to magnetron sputtering deposition

to obtain a resistive Ti/Pt and then a dual magnetron reactive sputtering to deposit piezoelectric ZnO coating [13]. Sandlin et al. investigated the method of coating FBGs with electroplating and brazing (Sandlin et al. 2006). However, this process showed some uncertainty with the uniformity of coating thickness around the fiber. Additionally, Iadicicco et al. showed that gold layer in nano-scale thickness can be deposited using evaporation technique in a vacuum chamber [14]. The resulting coated layer exhibited good uniformity and smooth interfaces. Another technique involving low temperature is electrowinning. For special application at cryogenic temperature ranges, Lupi et al. reported an increased FBG temperature sensitivity by coating FBGs with zinc and copper [15]. The technique involved the electrowinning process at room temperature for the deposition of the metallic layer after pre-coating the fiber with aluminum. The optical response could be tuned by adjusting the thickness of Zn coating to shift FBG peak, and thickness of copper to tune the peak width.

If the modulation of on-fiber coating was done in a periodic manner, the temperature and strain effects on the FBG could then be isolated following some of the techniques presented in 0. By covering half of the FBG with polymeric coating and the second half with another, simultaneous measurement of pressure and temperature was illustrated by the work from Liu et al. [47]. They reported a 30 fold increase in pressure sensitivity and 8 fold increase in temperature sensitivity. Using metallic coatings, Alemohammad & Toyserkani from our research group previously demonstrated the ability to deposit metalic films on on-planer fiber optic surface using the direct write method. Simultaneous measurement of temperature and tensile loading was demonstarted with a superstructure with a silver nano particle coating of the thickness of 9 μm [48].

2.6 FBG Packaging for Hash Environment

The use of FBG sensor has the notable advantage of low profile, electrically passive, and immunity to EMI, amongst a number of other advantages, compared to conventional electrical based sensors. This makes FBG sensors an ideal candidate for sensing applications in harsh environments. These harsh environments can be generalized to the

application-specific high temperature, high pressure, corrosive environment, or a combination of the aforementioned. This section aims to survey the available technology and packing techniques for harsh environment applications.

Zhang et al. proposed an ultrathin pressure sensor package design that involves a piston-like diaphragm [49]. The two ends of fiber were held by two flexible diaphragms. The center of the diaphragm was a copper piece to enhance sensitivity. On the other side of each diaphragm was an airtight cavity sealed with atmosphere pressure. Pressurized fluid entered and fills the cavity; diaphragms on both ends were deformed and finally induced mechanical strain on the fiber. This design unfortunately did not provide any protection to the fiber as the fiber was in direct contact with the external fluid, which in most harsh environments could be hostile and corrosive that could ultimately damage the fiber for prolonged exposure.

For practicality, a number of mechanical packaging designs were identified in the public US patent database. However, many of these designs consisted of the use of multiple strand of fiber optic sensor, closely spaced in the complex mechanical housing. Maron and Kersey proposed a multi-parameter sensor design for the particular use in harsh environment for the oil and gas industry [4]. The design composed an integrated structure for three separate FBG sensors, each use for temperature, pressure, and vibration sensing respectively. The FBGs are enclosed within a capillary tube made of a high strength, corrosion resistant material. To discriminate the effect to temperature and strain, Maron and Kersey illustrated different sections in the package design to allow a rigid reference element to provide temperature compensation. Similar designs involving a deformable main body for strain sensing by converting axial mechanical load, while a rigid and stationary temperature reference body is placed in vicinity, were also found in several patents [6], [18], [50], [51]. A notable design was the application of a bourdon tube demonstrated by Dunphy et al. [18] . The design involved delicate mechanical connects of a number of mechanical sub components. This design also involved the use of an additional FBG for temperature compensation, connected serially to the main FBG.

2.7 Summary

This chapter presents the fundamentals of fiber gratings and the various techniques in utilizing the grating structure for sensing applications. Due to the grating's sensitivity to both temperature and mechanical strain perturbation, reported techniques to discriminate the temperature and strain effects on the fiber are discussed. A review on packaging techniques for harsh environment showed that there is no simple and practical packaging solution that utilizes a single dual parameter FBG sensor with a compact profile.

3 Design, Fabrication, and Experimental Methods

From the literature review, there exist numerous coating techniques using a number of materials to achieve dual parameter sensing capability. Many of the existing fiber coating processes, however, are complicated, time consuming, costly, and not suited for mass production. The difference in material property of silica and metallic material also poses challenges for coating uniformity, consistency, and bonding reliability.

This chapter proposes a novel and economical coating design to achieve the simultaneous measurement of temperature and strain on an FBG.

3.1 Coating Design

The design proposed in this thesis involved the use of a metallic insert (needle) with inner diameter (ID) that is slightly (17 μm) larger than the cladding's outer diameter (OD) of a single mode fiber optic cable. The void between the inner diameter of the insert and the outer diameter of the fiber optic cladding was designed to be filled with an epoxy compatible for fiber optic bonding applications.

Similar to some of the designs found in literature [52], if the fiber is partially covered with an extra coated layer made of a different material, the effect of the temperature and strain imposed can be effectively discriminated.

This configuration implies a normal FBG is partitioned into two sections – with mismatches in diameter and effective coefficient of thermal expansion (CTE). The larger diameter at the coated section causes a decrease in force sensitivity due to the increase in cross sectional area and the difference in Young's modulus at the coating. Alternatively, the difference in CTE at the coated section causes a difference in thermal response as the coated section expands at a different rate, compared to the uncoated section.

As an initial investigation, half of the FBG is made covered by the insert for the ease of fabrication. A medical grade metallic needle is selected due to its low cost, commercial

availability, and high dimensional accuracy. Metallic needles are engineered with extremely high degree of precision for reduced drag forces during penetration [53], [54].

The goal for needle gauge selection was to minimize the gap between the ID of the needle and OD of the FBG. This is desirable to minimize the nonlinear effects of the epoxy. Table 3-1 shows three candidates of suitable needle gauge sizes [54].

Table 3-1 Suitable needle Gauge Chart

Gauge Size	Nominal Outer Diameter (μm)	Tolerance (μm)	Nominal Inner Diameter (ID) (μm)	Tolerance (μm)	Wall Thickness (μm)	Tolerance (μm)
29	336.6	±6.4	184	±19	76.2	±6.4
30	311.2	±6.4	159	±19	76.2	±6.4
31	260.4	±6.4	133	±19	63.5	±6.4

Gauge 31 has the closest match to fiber's OD of 125 μm. However, the only commercially available needle is gauge 30 with and ID of 159 μm. Therefore gauge 30 needle is selected as the metal insert, which implies the nominal gap size is $(159 - 125) / 2 = 17\ \mu m$.

To ensure a proper bonding of the needle with the silica surface, the selected epoxy was EPO-TEK 353ND - a two components thermal curing polymeric epoxy. 353ND was selected because of its proven compatibility with fiber optic application, high temperature operation, low viscosity, and high shear strength. The epoxy has reasonably low viscosity, 3000 cPs at 23°C, and high continues operating temperature of up to 250°C [55]. Since the gap between the insert and the fiber is exceptionally small, the low viscosity of the epoxy is ideal to warrant good flowability of the epoxy to fill all voids.

3.2 Fabrication/Assembly

The fabrication process for the proposed coated FBG involves three steps, the preparation of the insert, the preparation of the FBG, and thermal curing.

3.2.1 *Preparing the needle*

Figure 3-1 Needle a) as purchased b) detached.

The needle used is BD PrecisionGlide™ of gauge size 30 with a length of 12.5 mm (½ inch) as seen in Figure 3-1a. As received, the needle package includes the stainless steel cylinder body attached to a polypropylene hub. To remove the needle body from the polypropylene base, a metal file was used to slowly grind away material around the circumferences at where the metal meets the polypropylene. The grinding was continued until the needle cylinder detached from the base. Care was given to minimize deformation of the detached needle cylinder to avoid blockage of the ID of the needle body cylinder. A detached needle piece is shown in Figure 3-1b.

3.2.2 *Preparing the FBG*

The FBG used in all subsequent experiments was inscribed on a single mode fiber of the model Corning SMF-28. The FBG has an effective length of 10mm and the apodization function is a Gaussian function as defined in equation (4.19) . The section of the fiber where the FBG was inscribed has a polyimide coating, for added mechanical strength, as the original polymeric jacket was removed for the inscription of the FBG by the supplier. Since the FBG was not visible by eye, a blue mark was provided 20 mm from the center of the FBG by the supplier. One end of the fiber optic cable was connectorized with a FC/APC connector, while the opposite end was left unconnectorized.

Assembly Procedures:

1. Remove excess fiber from the unconnectorized end
2. From the unconnectorized end, use a mechanical stripping tool to strip the outer polymeric jacket to expose the fiber optic cladding

3. Place a microscopic plate under FBG
4. Brush the polyimide coated FBG using a cotton swab with furniture stripper until the coating is fully removed.
5. Carefully clean the exposed FBG with isopropanol using Kimwipes™
6. Prepare and mix the two part thermal curing epoxy
7. Use a small needle to apply small amount of epoxy to cover half of the FBG length
8. Slide the metal insert onto the FBG; ensure the epoxy uniformly flows into the gap between the insert and the fiber.
9. Position the insert such that it covers half of the FBG length

3.2.3 Thermal Epoxy Curing

The datasheet of epoxy 353ND has the generic specification for curing schedule with 150°C for 60 minutes. The glass transition temperature of the epoxy was reported as >90°C.

At below the glass transition temperature, the polymer behaves as a hard, glassy material. When the temperature reaches the glass transition temperature range, the polymer starts to soften and behaves similar to a rubbery material.

After several communications with EPO-TEK engineers, it was learnt that the glass transition temperature could be further optimized with a dynamic cure schedule. The optimized cure schedule is obtained as,

- Three steps of temperature set point: 80°C, 120°C, 150°C
- 30 minutes for each step

This enhanced glass transition temperature has a reported temperature in the range of ~120°C. Figure 3-2 shows the partially coated FBG after the thermal curing.

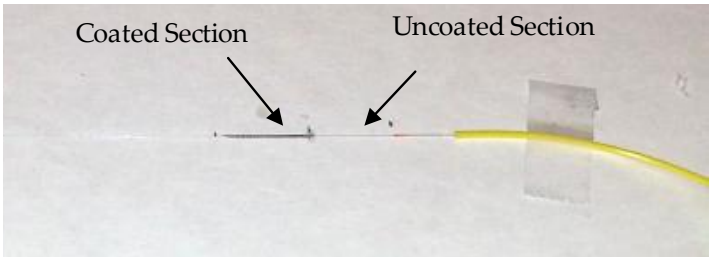

Figure 3-2 Coated FBG.

3.3 Effect of Thermal Residual Stress

A dynamic thermal curing process is adopted to maximize the glass transition temperature of the cure. Since the epoxy sets at a high temperature, there exists thermal residual stress within the coating structure as the cured coated fiber is brought back to room temperature. Figure 3-3 illustrates the optical spectrum of the coated FBG response versus the original response at room temperature.

Evidently, an extra peak became available after the thermal curing process. As the metal insert is made of stainless steel, it has a higher CTE value than silica. Assuming a solid bond at the epoxy layer is formed at high temperature, compressive stress/strain is induced within the coated section of the FBG as the temperature is reduced back to room temperature.

Since the uncoated section was not modified, the spectral response of the uncoated peak remained intact. The spectral response showed the newly created peak is ~1.2nm shifted from the original.

3.4 Calibration Setup

To fully understand the performance of the thin layer epoxy, a systematic setup to characterize the response of the proposed coated FBG is required.

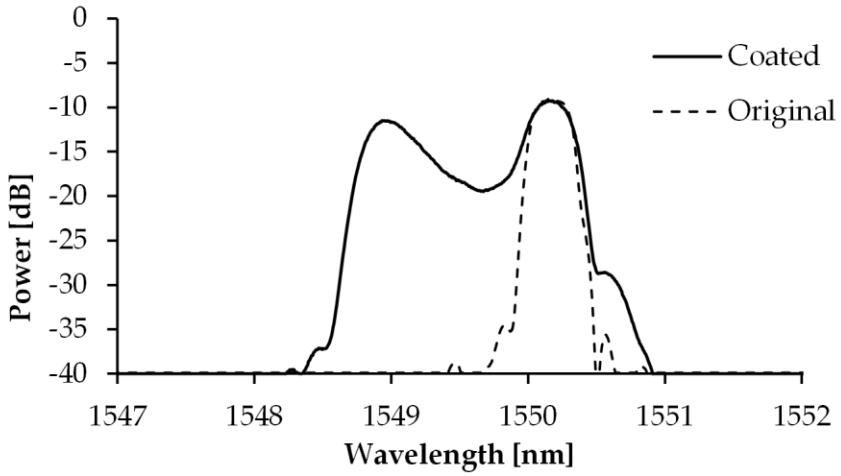

Figure 3-3 Thermally cured coated FBG compared with the original spectrum.

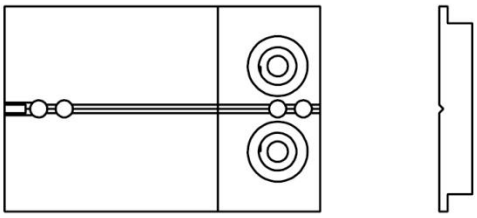

Figure 3-4 Top and side view of the flatplate package.

To this end, the optical fiber calibration setup previously developed in the research group was utilized [56]. To mount the fiber onto the calibration setup, a flatplate, made of Invar 36, mechanical package was used.

As seen in Figure 3-4, the flatplate package is made of two separate pieces. The design of the flatplate involves a small v-groove where the fiber optic will rest on. The center of the FBG is place at the center of the flatplate package. On each of the pieces, there are two circular epoxy pools to anchor the two ends of the FBG. As the epoxy has a fairly low viscosity, a second epoxy pool was designed to ensure the epoxy never overflow to the v-groove and end up bonding to the center of the FBG.

353ND-T, a sister epoxy product to 353ND, is used fill the epoxy pools for bonding the FBG to the flatplate package.

Table 3-2 Equipment list with accuracy and resolution specification

Equipment	Model	Accuracy	Resolution
Linear translation stage	Newport M-VP-25XA	1.0 μm	0.1 μm
Motion controller	Newport ESP 301		
Force Sensor	Thorlab FSC103/M	1 mN	1 mN
Force Sensor Reader	Thorlab TSG001		
Thermocouple Reader	NI USB 9211	1 μV	N/A
Thermocouple	OMEGA Type T	0.04 °C	N/A
DAQ	NI USB 6009	N/A	N/A
Optical Interrogator	Micron Optic sm125-200	10 pm	5 pm

It has similar thermal and mechanical properties compared to 353ND but with a higher viscosity, 9000 – 15000 cPs, which is favorable in this case to ensure the epoxy remains in place during the curing process.

In addition, the equipment used in the calibration setup is summarized in Table 3-2.

3.4.1 System diagram

Figure 3-5 shows the electrical connection of the fiber optic calibration setup. The thermocouple shown in the diagram is placed as closed as possible to the location of the FBG on the flatplate for measurement of the reference temperature. The reading of the thermocouple is also used for a closed feedback loop to control the heater for the thermal chamber.

Figure 3-6 shows the corresponding physical setup.

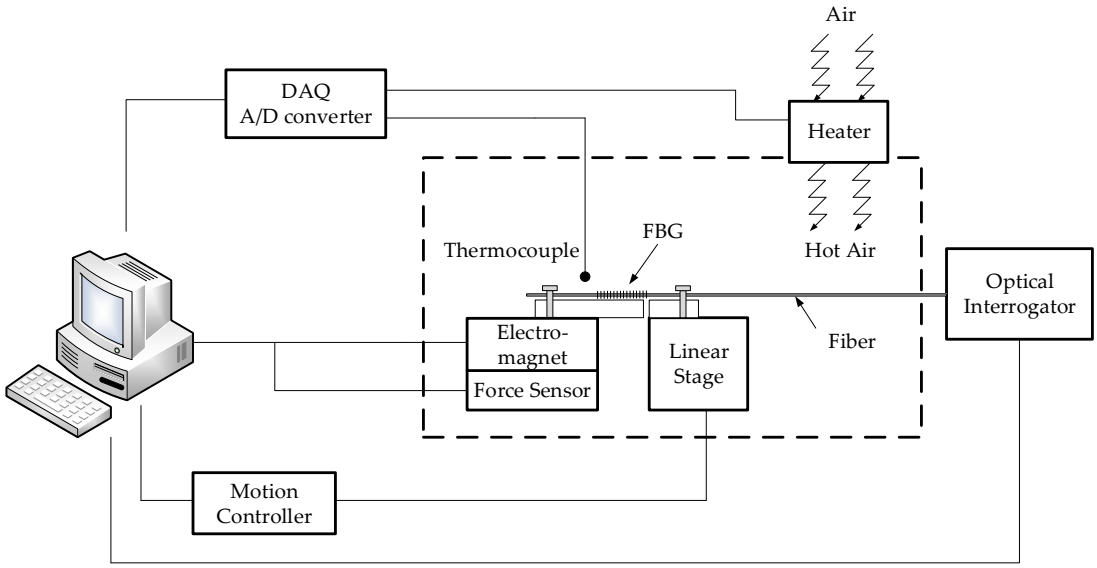

Figure 3-5 Block diagram of fiber optic calibration station.

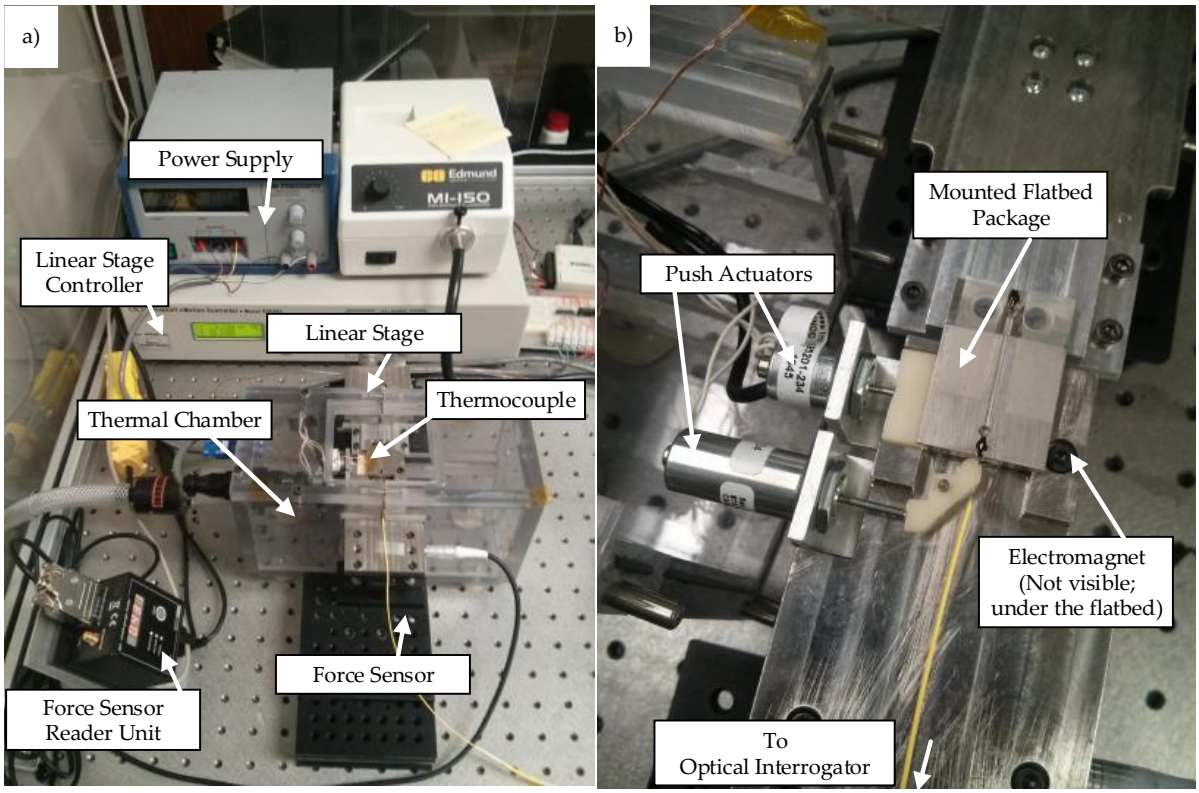

Figure 3-6 Calibration station in a) overall view b) detailed view.

3.5 Data Collection Procedure

In the past, the characterization of the fiber optic sensor was done manually. Each linear stage target position is entered one by one on the physical motion controller, while the temperature set points are set via a LabVIEW control panel, where the temperature control is implemented.

To minimize human error and ensure a high degree of repeatability of the experiment procedure, the LabVIEW software is fully expanded to interface programmatically to the force sensor and the motion controller. A unified LabVIEW application is developed to build the foundation for an automated fiber optic test rig.

A repetitive testing procedure is used for the analysis presented in Chapter 5. The procedure has the following steps,

1. Initialize linear stage and communication
2. Initialize force sensor reader
3. Set initial displacement (applied pre-tension)
4. Iterate temperature cycle ($T_{start}, \Delta T, n_{step}, t_{delay}$)
    a. Iterate displacement cycle ($d_{start}, \Delta \mathrm{d}, n_{step}, t_{delay}$)
5. Set number of cycles and repeat 3.
6. Close connection

Alternatively, the program flowchart is illustrated in Figure 3-7.

In parallel, a number of processes were also implemented in the LabVIEW program

- Digital temperature closed loop control
    - Update period: 0.5 second
- Display current system information
    - temperature, displacement set point, temperature set point, force sensor reading, optical spectrum reading
    - Update period: 2 second
- Save Sensor Data
    - Save optical spectrum

- System metadata: [date, time, force, temperature, linear stage position, cycle number, optical spectrum power]
- Save period: 1 second

3.6 Data Processing

Once the experiment had been completed, the data were transferred offsite for processing. This strategy was adopted to ensure the real time data collection in the experiment was done in a periodic manner. An offsite data processing has the added flexibility of experimentation of various data analysis techniques.

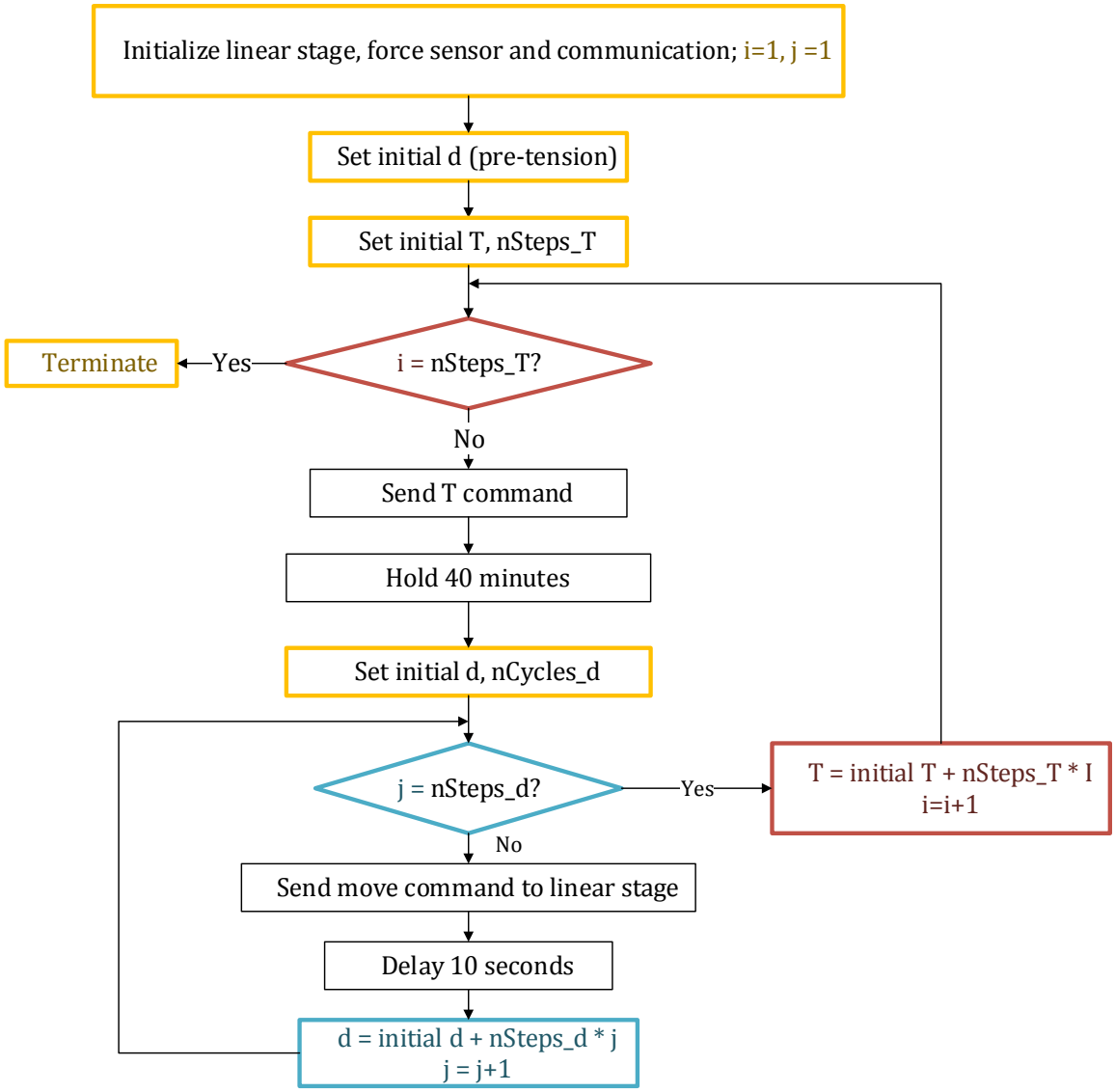

- **Figure 3-7 Testing procedure program Flowchart.**

This stage of data processing was implemented using MATLAB script to leverage its ease of use and large collection of analytical toolsets.

As seen in Figure 3-3, the thermal residual stress in the coated fiber section introduced a separate observable peak in the optical spectrum. To measure the shift in each of the peaks, the local maximas could be extracted and plotted against time. The measurements of peaks can be seen in red in Figure 3-8. However, there was a challenge in this method – at high enough temperature (approximately 110°C), the residual compressive stress due to thermal expansion mismatch would start to diminish - Peak 1 and Peak 2 would start to merged. Therefore, the algorithm to detect local maxima would begin to become unstable. The detection of local maximas was deemed to introduce false detections. Many local maxima, with much lower power levels, were observed near the main reflective peak, as seen in Figure 3-9. In addition, their locations and peak level drifted over time due to the noise in the optical interrogator,

To resolve these issues, a level crossing technique was adopted as demonstrated in dashed lines in Figure 3-9. It was found that the spectral width of each of the peak remain constant for the span of the measurement range selected in this thesis. Therefore, the level crossing method was deemed practical and accurate as long as consistent level is selected. At each time step, the wavelength value(s) of where the spectral response crossed a particular power level were recorded. The value of -29 dB was selected arbitrarily and this method has shown consistency in further analysis as presented in Chapter 5.

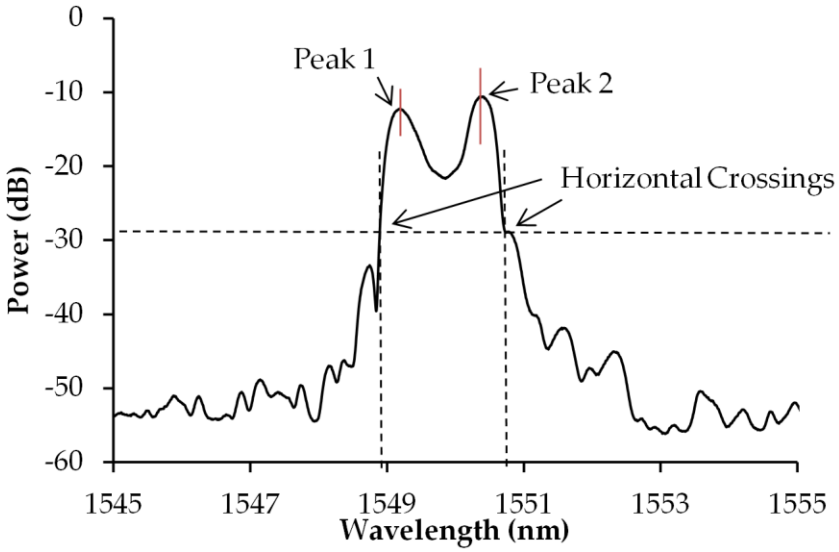

Figure 3-8 Measurement technique of the coated FBG spectral response.

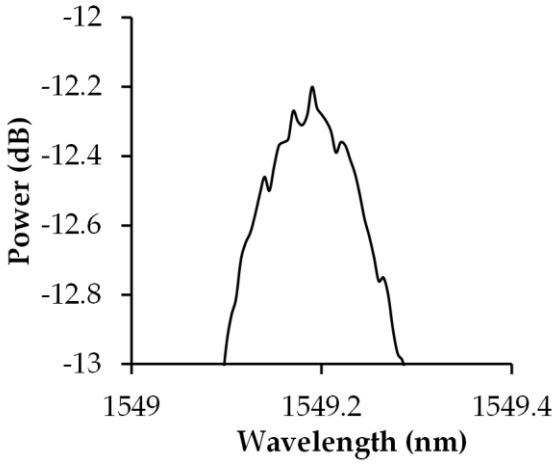

Figure 3-9 Detailed view of spectral response at Peak 1.

3.7 Summary

A novel design involving a metal insert, with ID of 159 μm and OD of 311 μm, and a two component thermal epoxy is presented. The assembly process is simple but delicate and requires a dynamic curing schedule to maximize the thermal epoxy's glass transition temperature. The curing process for the thermal setting epoxy induces a substantial thermal residual stress in the coated FBG, hence a secondary FBG peak corresponding to the coated section of the FBG is observed. The calibration setup used to validate the performance of the coated FBG is presented along with a data collection and data processing scheme.

4 Analytical Model

To fully understand the optical and mechanical response of a coated FBG, this chapter presents the adaptation and integration of an opto-mechanical model. The model presented here is solved by a FEM model developed in COMSOL Multiphysics® and a differential equation solver developed in MATLAB.

4.1 Couple Mode Theory

The couple mode theory provides the necessary mathematical formulation with excellent accuracy in predicting FBG's optical response. The derivation here follows closely to the one use by Erdogan [57], where the notation is first formulated by Kogelnik [58].

For an electromagnetic wave propagating inside a waveguide, we can start by writing the slowly varying amplitude function of the forward propagating mode $R(z)$ and the backward propagating mode $S(z)$,

$$R(z) \equiv A(z) \exp\left(i\delta z - \frac{\phi}{2}\right) \tag{4.1}$$

$$S(z) \equiv B(z)\exp(-i\delta z + \frac{\phi}{2}) \tag{4.2}$$

where δ is the detuning function, ϕ is the grating chirps, and z is the longitudinal position on the fiber.

The amplitude functions must obey the following differential equations [57],

$$\frac{dR}{dz} = -i\hat{\sigma}R(z) - i\kappa S(z) \tag{4.3}$$

$$\frac{dS}{dz} = +i\hat{\sigma}S(z) + i\kappa R(z) \tag{4.4}$$

where κ is the "AC" coupling coefficient and $\hat{\sigma}$ is the "DC" self-coupling coefficient,

$$K_{AC} = \kappa = \frac{\pi}{\lambda} v_f \overline{\delta n_{eff}} \tag{4.5}$$

$$K_{DC} = \hat{\sigma} \equiv \delta + \sigma - \frac{1}{2}\left(\frac{d\phi}{dz}\right) \tag{4.6}$$

v_f is the fringe visibility of the grating chirp, $\overline{\delta n_{eff}}$ is the average refractive index change or "DC" change over the grating length, σ is the period-averaged coupling coefficient,

$$\sigma = \frac{2\pi}{\lambda} \overline{\delta n_{eff}} \tag{4.7}$$

δ is the detuning function,

$$\delta = 2\pi n_{eff} \left(\frac{1}{\lambda} - \frac{1}{\lambda_B}\right) \tag{4.8}$$

Substituting (2.2) into (4.8) we obtain,

$$\delta = \frac{2\pi n_{eff}}{\lambda} - \frac{\pi}{\Lambda} \tag{4.9}$$

Finally, we can obtain the generalized DC coupling coefficient by substituting (4.7) and (4.9) into (4.6),

$$\hat{\sigma} = \frac{2\pi n_{eff}}{\lambda_B} - \frac{\pi}{\Lambda} + \frac{2\pi}{\lambda_B} \overline{\delta n_{eff}} - \frac{1}{2}\left(\frac{d\phi}{dz}\right) \tag{4.10}$$

For common FBG with uniform gratings, this implies $\overline{\delta n_{eff}}$ is constant and $d\phi/dz = 0$.

The two differential equations (4.3) and (4.4) can be reduced into a coupled first-order ordinary differential equations with constant coefficients. Therefore, a closed form solution can be obtained, provided appropriate boundary conditions are given.

Grating functions on FBGs can be apodized to suppress side lobes [57]. Following the definition of the common apodization functions in (4.19) and (4.20), it would be convenient to define a coordinate system where the centre of the FBG has the maximum

refractive index. This centre therefore will correspond to $z = 0$. Assume the FBG have an arbitrary length L and centered at 0 such that the grating's edge is located at $L/2$ and $-L/2$.

If a propagating wave originated from $-\infty$ and enters the grating at $z = -L/2$, then the boundary condition at the Bragg wavelength (λ_G) can be defined as

$$R(-L/2) = 1$$
$$S(L/2) = 0$$

which means the forward propagating mode at grating entrance is 100% and there is 0% backward propagating mode at the end of grating.

We can simplify the pair of differential equations, (4.3) and (4.4), by introducing a new function $\rho(z)$ to denote the reflectivity of the grating in the form of a ratio,

$$\rho(z) = \frac{S(z)}{R(z)} \tag{4.11}$$

Taking the derivative with respect to z using chain rule,

$$\frac{d\rho(z)}{dz} = \frac{1}{R(z)}\frac{dS(z)}{dz} - \frac{\rho(z)}{R(z)}\frac{dR(z)}{dz} \tag{4.12}$$

Substituting (4.3) and (4.4) into (4.12),

$$\frac{d\rho}{dz} = \frac{1}{R}(i\hat{\sigma}S + i\kappa R) - \frac{\rho}{R}(-i\hat{\sigma}R - i\kappa S) \tag{4.13}$$

Rearranging and substituting again

$$\frac{d\rho}{dz} = \left(\hat{\sigma}\frac{S}{R} + \kappa + \rho\hat{\sigma} + \kappa\rho\frac{S}{R}\right)i \tag{4.14}$$

Since $S/R = \rho$,

$$\frac{d\rho}{dz} = (\kappa\rho^2 + 2\hat{\sigma}\rho + \kappa)i \tag{4.15}$$

For non-uniform gratings, we can recognize that $\kappa, \hat{\sigma}$ are both function of z and $\overline{\delta n_{eff}}$ varies along the fiber axis, substituting (4.5) and (4.6) into (4.15) and only considering the imaginary component,

$$\frac{d\rho}{dz} = \left[\left(\frac{\pi}{\lambda}\nu_f\,\overline{\delta n_{eff}}\,(z)\right)\rho^2 + 2\left(\frac{2\pi n_{eff}}{\lambda} - \frac{\pi}{\Lambda} + \frac{2\pi}{\lambda}\overline{\delta n_{eff}}(\mathrm{z})\right)\rho + \frac{\pi}{\lambda}\nu_f\,\overline{\delta n_{eff}}(z)\right]i \tag{4.16}$$

(4.16) is a first order differential equation that is quadratic with the unknown function – also known as the Riccati function. This can be solved by using numerical methods of a 4th order Runge-Kutta algorithm [59].

To apply the Runge-Kutta numerical solver for the Riccati differential equation presented in (4.16), the MATLAB script initially developed by Alemohammad [60] is adopted for the modelling and analysis presented in this chapter, see Appendix A for the source code.

Integration is done backwards from $= L/2\ to\ -L/2$. Since $S(L/2) = 0$ and using (4.11), we define the equivalent boundary condition as,

$$\rho(L/2) = 0 \tag{4.17}$$

The reflected amplitude is then solved by obtaining $\rho(-L/2)$. Finally, the reflective power is the square of the reflected amplitude at each specific wavelength, namely,

$$r(\lambda) = \left|\rho\left(-{}^{L}/_{2}\right)\right|^2 = \left|\frac{S(-L/2)}{R(-L/2)}\right|^2 \tag{4.18}$$

4.2 Apodization of Fiber Grating

FBG with uniform grating pitch exhibits a series of side lobes adjacent to the main Bragg wavelength in the reflected spectrum. It is important to supress such side lobes to ensure

only narrow band of the resonant wavelengths are reflected. Side lobes can be suppressed by introducing a non-uniform apodization profile along the length of the grating [2]. In this case, the average refractive index is no longer simple periodic.

The two typical apodization functions are Gaussian and Raised-Cosine types [57]. Gaussian apodization takes the form,

$$\overline{\delta n_{eff}}(z) = \overline{\delta n_{eff}} \exp\left(-\frac{4\ln(2)\, z^2}{FWHM^2}\right) \tag{4.19}$$

where $\overline{\delta n_{eff}}$ is the average or "DC" effective index change, FWHM is the Full-Width-Half-Maximum of the apodization function, z is the location along the fiber axis.

Raised-cosine takes the form,

$$\overline{\delta n_{eff}}(z) = \overline{\delta n_{eff}} \frac{1}{2}\left[1 + \cos\left(\frac{\pi z}{FWHM}\right)\right] \tag{4.20}$$

4.3 Mechanical Modelling

A finite element methods (FEM) model is developed in COMSOL Multiphysics to model the structural effects of the fiber under thermal and tensile loading. The resultant strain calculation of this model is then coupled with the opto-mechanical model in MATLAB to predict the optical performance of the coated FBG.

Figure 4-1 illustrates the geometry, dimension not to scale, used in the FEM model. Axial symmetry model is implemented to reduce computational load. The inputs of the FEM model are defined to be consistent with the temperature set point and force measurements from experiment.

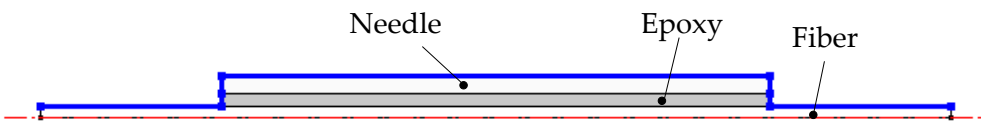

Figure 4-1 Cross section of the coating bilayer on the FBG.

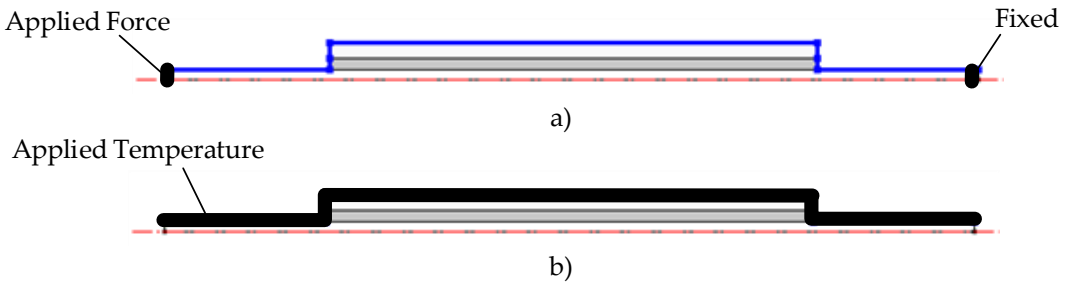

Figure 4-2 a) Structural and b) thermal boundary conditions applied.

To account for the displacement error and structural movements in the calibration setup, displacement set points are not used as reference in the model. The boundary conditions in the model are set as illustrated in Figure 4-2.

Table 4-1 summarizes the material properties used in the FEM model. Every attempt is made to ensure the material property is appropriately estimated by a combination of the supplier's data and literature.

A few simplification and assumptions are made for this preliminary FEM model:

1. Material property does not vary significantly with temperature for the range of 30-110°C.
2. The heating of the FBG package is uniform
3. Axial tensile force F is perfectly perpendicular to the transverse plane of the fiber
4. Epoxy used to anchor the FBG package to the flatplate remains rigid as it is not included in the model

4.4 Opto-mechanical Modelling

An FBG's sensing ability stems from the change of effective refractive index of the optical fiber and the grating period of the gratings, under external perturbation in applied mechanical load and/or in temperature. Fiber optic is made of silica which is a dielectric material. Dielectric material possesses the optical properties that are coupled with mechanical properties called the optomechanical properties. In an FBG, there are two mechanisms that affect the reflected Bragg wavelength [17],

Table 4-1 Constants for FEM Model

Material	Thermal conductivity ($W \bullet m^{-1} \bullet K^{-1}$)	Heat capacity ($J \bullet kg^{-1} \bullet K^{-1}$)	Coefficient of Thermal Expansion (1/K)	Poisson's Ratio	Young's modulus (GPa)	Density (kg/m^3)	Reference
Epoxy (EPO-TEK 353ND)	40	930	54.0E-6	0.3	10	1100	[55], [61], [62]
Stainless Steel (SS-304)	16.2	475	9.4E-6	0.28	193	8030	[63]
Fiber Optic (Silica Glass)	1.38	703	550.0E-9	0.17	73	2203	[16], [64], [65]

- **Mechanical perturbation**: applied mechanical load directly affects the pitch between gratings (Λ_G) and the effective refractive index (n_{eff}) through strain-induced photo-elastic effect [38].
- **Temperature perturbation**: change in temperature affects the refractive index due to thermo-optic effect, as well as the thermal expansion, to a lesser extent, of the dielectric material.

The change in refractive index of the dielectric material silica under both mechanical and thermal loading can be described as [66],

$$\Delta n_{eff} = -\frac{n_{eff}^3}{2}\left[(p_{11}+p_{12})\Delta\epsilon_2 + p_{12}\Delta\epsilon_1 - \frac{2}{n_{eff}^3}\left(\frac{\partial n}{\partial T}\right)\Delta T - (p_{11}+2p_{12})\alpha\Delta T\right] \quad (4.21)$$

where $\Delta\epsilon_1$is the axial strain, $\Delta\epsilon_2$is the traverse strain, p_{11}, p_{12} are the pockel's photo-elastic constant components, $\frac{\partial n}{\partial T}$ is the sensitivity of refractive index with temperature,

The formulation of Δn_{eff} in equation (4.21) can be incorporated and rewritten to return the shift in Bragg wavelength [60],

$$\frac{\Delta\lambda_B}{\lambda_B} = \Delta\epsilon_1 - \frac{n_{eff}^2}{2}[(p_{11}+p_{12})\Delta\epsilon_2 + p_{12}\Delta\epsilon_1] + \frac{1}{n_{eff}}\left(\frac{\partial n}{\partial T}\right)\Delta T + \frac{n_{eff}^2}{2}(p_{11}+2p_{12})\alpha\Delta T \quad (4.22)$$

Table 4-2 Constants for the optical model

Parameter	Value
v_f	5
$\overline{\delta n_{eff}}$	1×10^{-5}
$FWHM$	3.33
n_{eff}	1.4487
$\lambda_B\ (nm)$	1550.125
$\Lambda\ (nm)$	*535*
α_f	0.55×10^{-6}
$\partial n/\partial T$	1.2×10^{-5}
$L_G\ (mm)$	10

Poisson's ratio determines the proportion of the transvers strain to axial strain,

$$\epsilon_2 = -v\epsilon_1 \tag{4.23}$$

Equation (4.22) can be rearranged into a function $\Delta\lambda_B$ that depends on $\Delta\epsilon_1$ and ΔT. Substituting (4.23) into (4.22) and simplifying,

$$\Delta\lambda_B = \left[1 + \frac{n_{eff}^2(p_{11}+p_{12})v}{2} - \frac{n_{eff}^2}{2}p_{12}\right]\lambda_B\,\Delta\epsilon_1 + \left[\frac{2}{n_{eff}}\frac{\partial n}{\partial T} + \frac{n_{eff}^2}{2}(p_{11}+2p_{12})\alpha\right]\lambda_B\Delta T \tag{4.24}$$

Table 4-2 shows the optical constants used for solving the differential equation. The combined opto-mechanical model utilizing both mechanical and optical model can be illustrated in **Figure 4-3.**

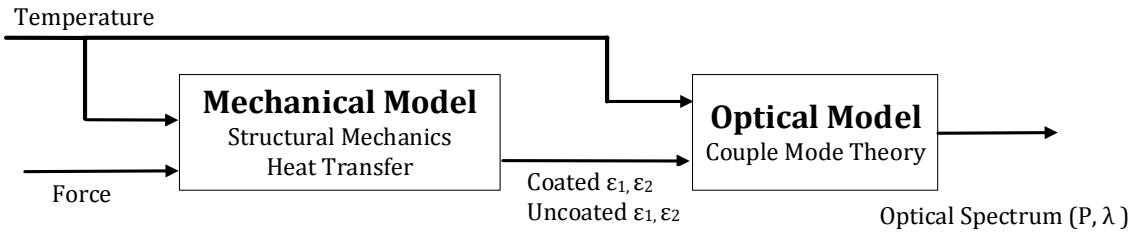

Figure 4-3 Opto-mechanical model connection diagram

4.5 Dual Parameter Calibration Matrix

Since both temperature and strain affects the optical response of an FBG, it is important to formulate the decoupling function, given the shifts of Bragg wavelengths in a coated fiber. This section's derivation follows closely with the work found in literature [8], [9], [67].

For the FBG with half of the length coated with a different material, a second function of the form equation (4.24) can be written for two measurable Bragg wavelengths. Let the first wavelength (λ_{B_1}) be the coated section, which is strongly coupled to the temperature effect; and the second wavelength (λ_{B_2}) be the uncoated section, which is strongly coupled to the strain effect. The two equations with the form presented as (4.24) can be written into a simplified matrix form,

$$\begin{bmatrix}\Delta\lambda_{B_1}\\ \Delta\lambda_{B_2}\end{bmatrix} = \begin{bmatrix}K_{T_1} & K_{\epsilon_1}\\ K_{T_2} & K_{\epsilon_2}\end{bmatrix}\begin{bmatrix}\Delta T\\ \Delta\epsilon\end{bmatrix} \tag{4.25}$$

where K_{T_1} and K_{ϵ_2} represent the strong coupling effect and K_{ϵ_1} and K_{T_2} represent the weak coupling effect (or cross axis coupling) of the respective Bragg wavelength.

Let the square matrix be the sensitivity matrix $[K_1]$,

$$[K_1] = \begin{bmatrix}K_{T_1} & K_{\epsilon_1}\\ K_{T_2} & K_{\epsilon_2}\end{bmatrix} \tag{4.26}$$

Taking the inverse of matrix $[K_1]$, we obtain $[K_1]^{-1}$,

$$\begin{bmatrix}\Delta T\\ \Delta\epsilon\end{bmatrix} = \frac{1}{D}\begin{bmatrix}K_{\epsilon_2} & -K_{\epsilon_1}\\ -K_{T_2} & K_{T_1}\end{bmatrix}\begin{bmatrix}\Delta\lambda_{B_1}\\ \Delta\lambda_{B_2}\end{bmatrix} \tag{4.27}$$

where $D = K_{\epsilon_2}K_{T_1} - K_{T_2}K_{\epsilon_1}$, assuming matrix K is not singular - $D \neq 0$

4.6 Model Validation

The validation of the structural model and couple mode theory is presented here. All sensor measurements are collected using the optical calibration station presented in

Section 3.4. The data collection and processing procedures are followed as described in Section 0 and 3.6. Temperature and strain effects on the FBG are individually addressed in the following subsections.

4.6.1 Applied Temperature

For the temperature performance of the sensor, a total of four temperate set points were investigated $-30 \pm 0.5°C,\ 50 \pm 1.0°C,\ 70 \pm 1.9°C,\ 90 \pm 2.5°C$. Due to the thermal chamber's limitation, all measurements were made at steady state after 40 minutes of settling time. Further dynamic analysis of the setup can be found in section 5.1.

The strain from the coated and uncoated section of the FBG was first calculated from the finite element model. The strain calculation was then entered into the differential equation solver developed in MATLAB. Figure 4-4 illustrates the spectral response of the coated FBG, comparing the experimental result with the modelling result.

As we are not concerned with the intensity of the reflected spectrum, all reflected power measurements are normalized for better side-by-side comparison.

The difference in power level of each peak was the result of assembly variations of the metallic insert. During the assembly process, the metallic insert was carefully slid onto the FBG, together with a layer of epoxy, until the insert's edge is aligned with the centre mark of the FBG. This process was manual and it consisted of human error in the final coating position. Also, the thermal curing epoxy was cured by resting the coated FBG on a hotplate. It had been observed that the insert could move slightly off-centre due to the uneven surface of the hot plate, or due to the dynamics of the epoxy. For the optical response in model, the difference in optical intensity of the two peaks was empirically determined to match with the experimental result. The modelling result in Figure 4-4 has an offset value of -0.3 mm.

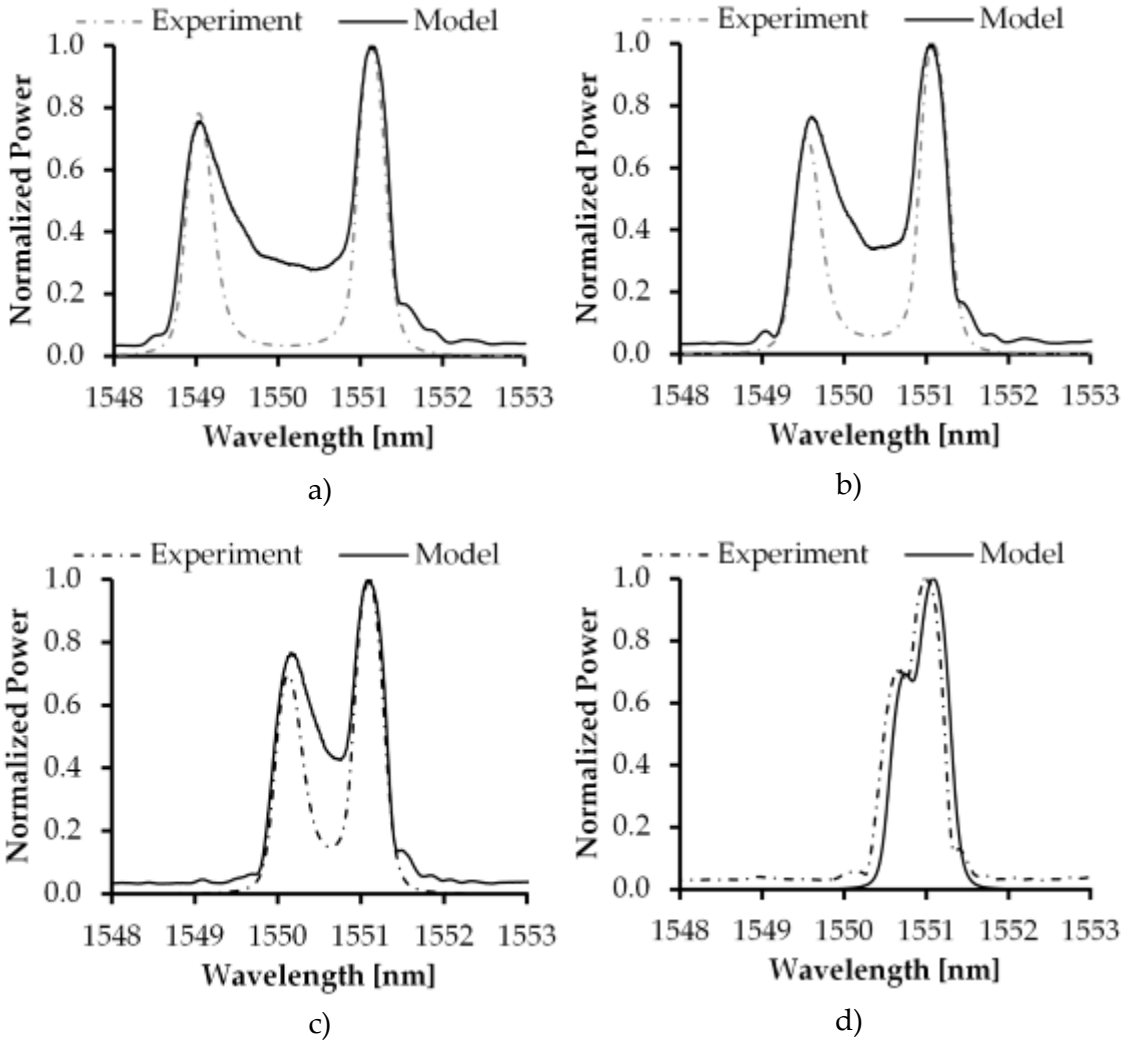

Figure 4-4 Normalized optical spectrum of model vs experiment at a) 30°C b) 50°C c) 70°C d) 90°C.

The experiment and modelling results showed excellent agreement from 30°C to 70°C. This validated the coefficient of thermal expansion used in the modelling for epoxy, and the coating material. At higher temperature of 90°C, the shape of the spectral response continued to match; however, a small discrepancy started to become evident. Compared to the model, the spectral response from experiment was slightly lower. This discrepancy could be described by the effect of the epoxy used to anchor the FBG onto the flatplate package, which was not modelled in FEM. These effects could be mostly attributed to the increase in CTE of the epoxy and the decrease of Young's modulus as the temperature was raised close to the glass transition temperature of the epoxy.

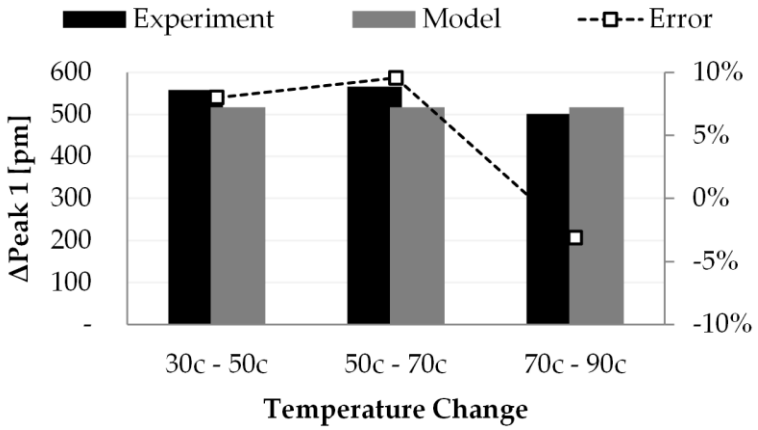

Figure 4-5 Bragg wavelength Peak 1 shift at different temperature transitions.

The increase in CTE was expected to dominate as the glass transition temperature was expected to be 120°C, following the thermal curing schedule outlined in section 3.2.3.

The expansion of the epoxy introduced an additional relative displacement between the fiber and the flatplate, which reduced the overall mechanical strain experienced by the FBG. This explains the lower peak wavelengths seen at 90°C, as shown in Figure 4-4d.

Combining the strain calculated from FEM model and the opto-mechanical model from equation (4.24), Figure 4-5 shows the wavelength shift has a reasonable agreement with the experimental result, with a maximum error of 10%.

4.6.2 Applied Strain

Seven displacement steps were used to apply the tensile force cycles on the coated fiber. At each step, a change of 5 μm was applied. Each measurement was made after 10 seconds of settling time. The temperature was held at 30 ± 0.1 °C in the thermal chamber.

In the spectral response shown in Figure 4-6, it was evident that the sensitivity of the uncoated FBG (Peak 2) to applied mechanical axial strain was much higher than the coated section (Peak 1). Figure 4-6a shows the detailed view of the minor wavelength shift at Peak 1. Figure 4-6b shows the shift experienced by Peak 2 is much higher in comparison.

To validate the proposed opto-mechanical model, Figure 4-7 shows the comparison of the modelled spectral response with experimental result at the two extreme cases.

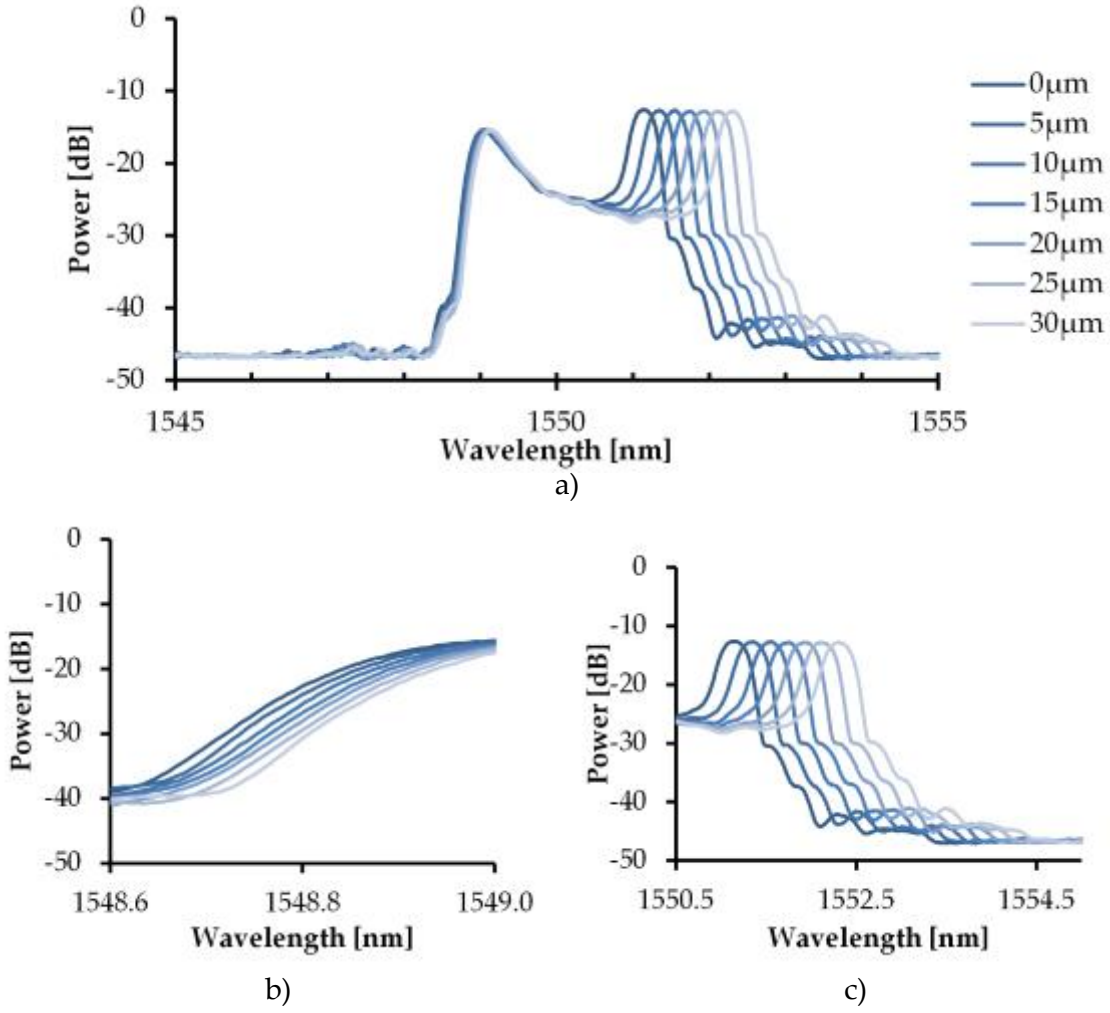

Figure 4-6 Spectral response of the FBG at different displacement.

At low displacement/strain, the model response seemed to have a lower prediction of the Peak 2; however, a much better fit was obtained at high displacement, as shown in Figure 4-7b. In addition, it was observed that the model had predicted a decrease of Peak 1's reflectivity relative to Peak 2 as the displacement level was increased.

As seen in Figure 4-5, the model was accurate in predicting the Peak 2 wavelength shift at each of the displacement level. The amount of modelling error was within ± 5% except at displacement of 20 μm. As the force measurement from the experiment was used as the boundary condition input for the simple FEM model, the discrepancy in the opto-mechanical model could be attributed to the measurement errors from the force sensor.

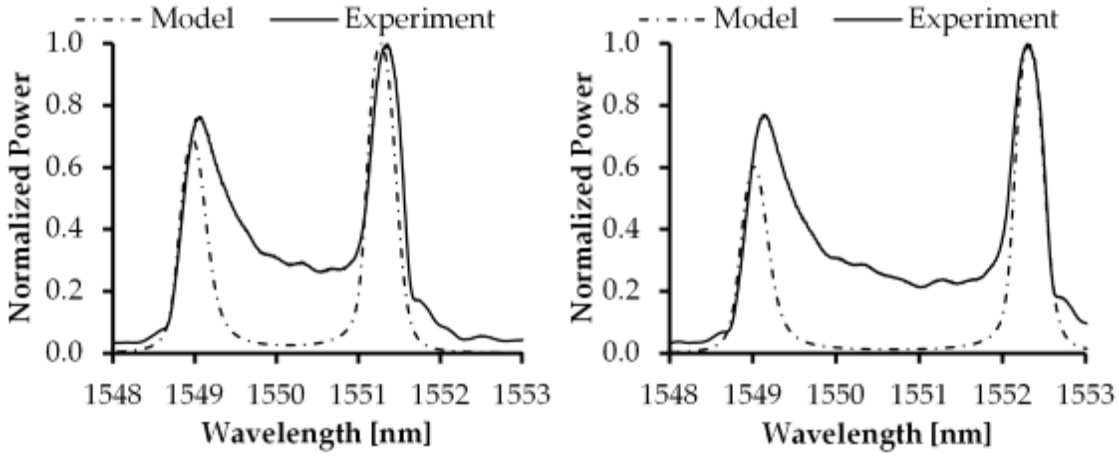

Figure 4-7 Normalized optical spectrum of modelled vs experiment at a) 5 μm and b) 30 μm displacement.

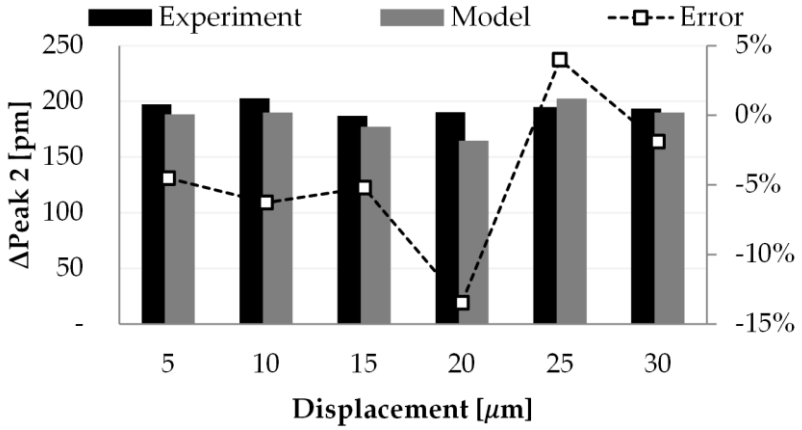

Figure 4-8 Bragg wavelength Peak 2 shift at different displacement level.

4.7 Summary

This chapter presented an overview of the mathematical formulation of the optical model for FBG using the couple mode theory. Following the work previously completed at the research lab, an opto-mechanical model consisted of a mechanical FEM model and an optical model using the couple mode theory was presented. To analyze the effect of the added layer of epoxy and the metallic insert, a FEM model was developed in COMSOL Multiphysics. The mechanical modelling result from FEM was then used to complement the existing optical model developed in MATLAB. The model was validated and the modelling error is reported to fall within 10% for temperature and 15% for strain.

5 Experimental Results and Analysis

This chapter presents an in-depth analysis of proposed implementation of the coated FBG. Since a polymeric epoxy is chosen as the bonding agent between the insert and the FBG, the effect on the response of the coated FBG should be studied. This chapter presents the sensitivity of the sensor at a number of temperature set points, as well as tensile loading levels. The discrepancies observed in the experimental results are documented and discussed.

5.1 Dynamic Response

Since the FBG being investigated was mounted in a custom thermal chamber with a large thermal mass, the dynamic response of the sensor system must be understood to assess the temperature performance of the sensor. Figure 5-1 shows the measured FBG response along with the reference temperature measured by the thermocouple.

It was evident that the FBG has a slower response time compared to the reference thermocouple.

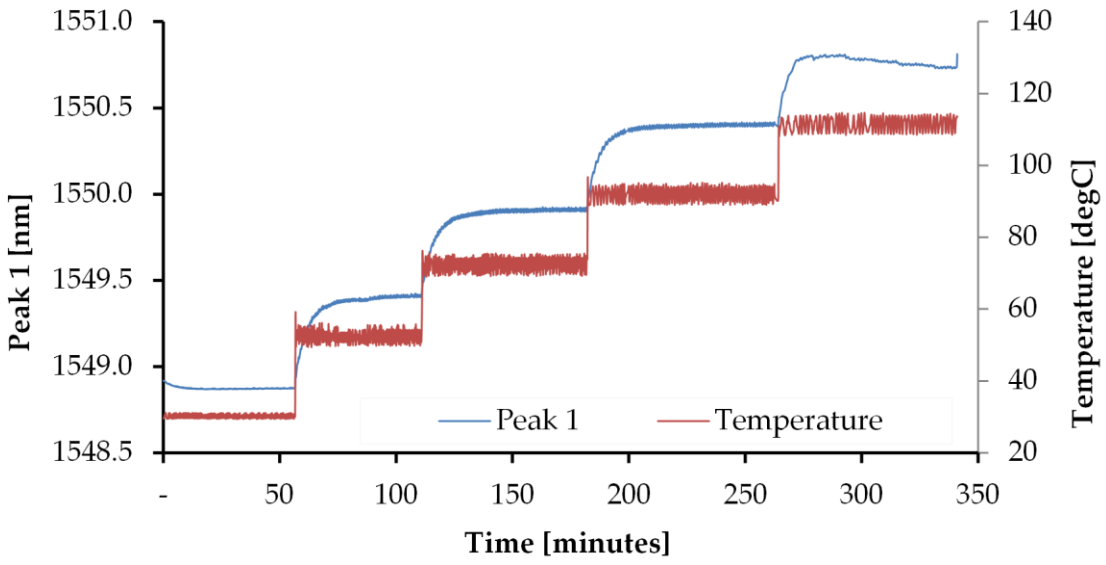

Figure 5-1 Time response of sensor Peak 1 vs thermocouple reference temperature.

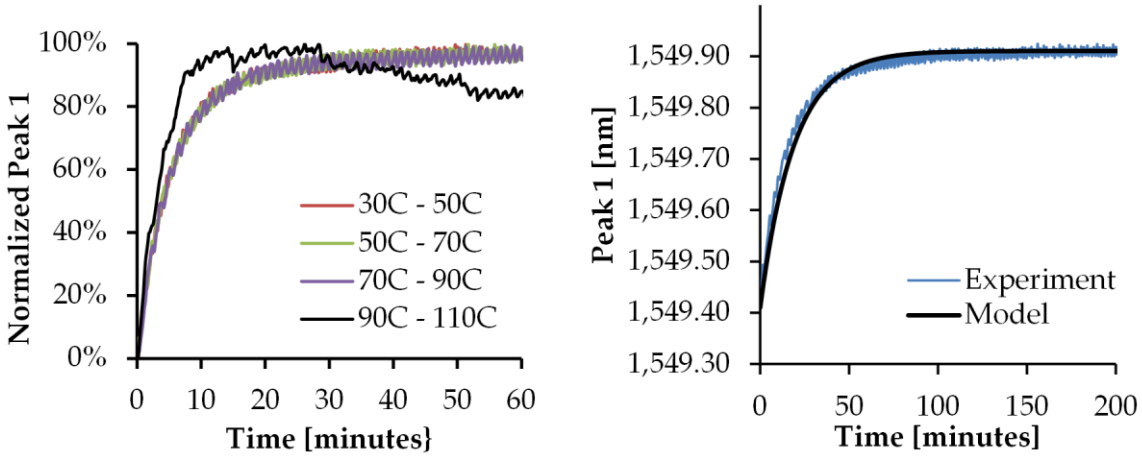

Figure 5-2 a) Normalized FBG response to temperature b) FBG Peak 1 response vs model.

Although the thermocouple was placed as close as possible to the FBG under test, the thermocouple exhibited a much smaller thermal mass; the FBG, in contrary, was mounted on a flatplate, which the two ends were anchored to two separate and large metal bodies – the force sensor and the linear translation stage. A large proportion of these two metal bodies were also placed outside of the thermal chamber, where the interfacing environment temperature was at ambient room temperature.

Isolating each of temperature step response and normalizing the FBG output value, Figure 5-2a shows similar response of the FBG sensor to the temperature step input excitation, for the range between 30°C to 90°C.

The response of the FBG Peak 1 response with temperature step input followed a first order response. The first order response of a step input can be approximated by an exponential function of the following form,

$$\lambda_1 = \Delta\lambda \left(1 - e^{-t/\tau}\right) + \lambda_0$$

where λ_1 is the new Peak 1 location, $\Delta\lambda$ is the DC gain, τ is the time constant, and λ_0 is the initial Peak 1 location. Figure 5-2b illustrates the response of the FBG when temperature was increased from 30°C to 50°C. The time constant, which is defined as the time to reach $1 - 1/e = 63.6\%$, is approximately 10 minutes by visual inspection. The black line in Figure 5-2b is the modelled dynamic response with a good fit.

To ensure the FBG is fully settled, a delay time of $4\tau = 40\,minutes$ at each change of temperature. The long settling time for the FBG's temperature response could be attributed to the limitation of the existing experimental setup:

- Insufficient thermal power from the heater,
- Lack of proper thermal insulation,
- High thermal mass of the linear translation stage, exposed to external environment,
- Heat conduction through the electrical wire connected to thermocouple and electromagnet, as well as the screws and nuts.

For the temperature step input from 90°C to 110°C, however, the FBG seemed to exhibit a higher order response. This added complexity in transient state could be explained by continued softening of the epoxy at elevated temperature, which is also closed to the glass transition temperature of this epoxy. Hence, only the steady state should be considered for characterization of the coated FBG sensor.

Investigating the transient response of the FBG further, Figure 5-3 shows the Peak 1 response under a tensile loading/unloading cycle. As seen, the zero reference of Peak 1 shifted about 10 pm after 3 repetitions of cyclic loading. Since Peak 1 corresponds to the coated region of the FBG, the slow upward shift can be explained by the slow internal heating of the FBG under the first few cycles of tensile loading.

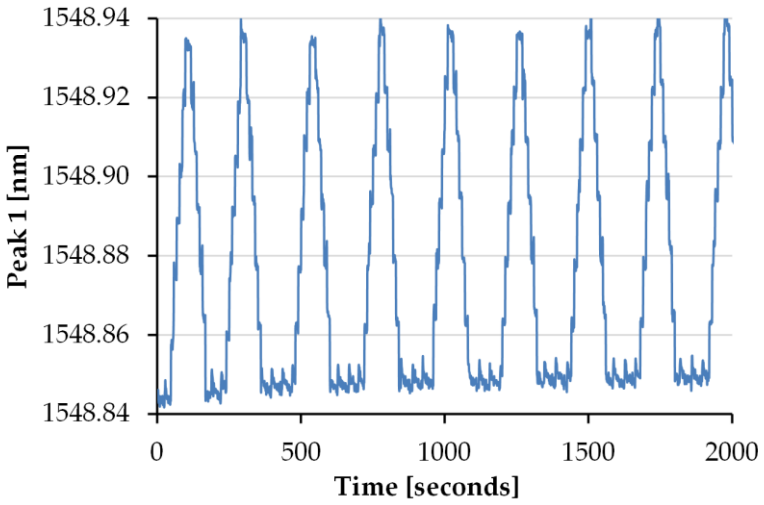

Figure 5-3 Peak 1 response under tensile force cycle.

5.2 Characterization

If the calibration station was given the time to settle to equilibrium, the performance of the sensor at each of the steady states could then be appropriately analyzed. The following analysis discusses the characterization process separately with temperature and mechanical load.

5.2.1 Sensitivity to Temperature

Figure 5-4 shows the shift in Peak 1 with respect to the measured reference thermocouple temperature. Higher fluctuation is evident at higher temperature as previously seen in Figure 5-1. This fluctuation was caused by the temperature controller's inability to hold a steady state temperature. Fluctuation of up to ±2.5 °C at $T_{set} = 90\ °C$ is observed. The linear curve fit has a rather satisfactory fit with a coefficient of determination of 0.9944. Using the curve of best fit, the temperature sensitivity of the coated FBG is $26.9 \pm 0.3\ pm/°C$. The improved sensitivity is almost 2.7 times higher than that of a bare fiber, which is $10\ pm/°C$ [1].

It should be noted that there is a higher fluctuation in optical response from the coated FBG. At high temperature, maximum fluctuation seen in Peak 1 is a total of 0.2 nm, which corresponds to a total of 7.1 °C, almost three times as high as the fluctuation seen by the reference thermocouple.

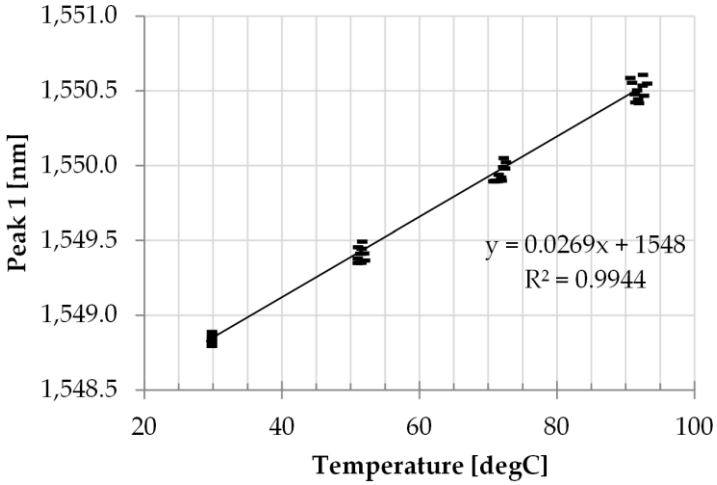

Figure 5-4 Optical response of Peak 1 related to temperature.

The higher temperature fluctuation in the FBG showed the limitation of the calibration station configuration. The coated fiber rests on a v-groove on the flatplate package. Each end of the package was in direct contact with two mounting plates extending outside of the thermal chamber. Each of the mounting plates was attached to large thermal masses – linear translation stage and the force sensor. These two large thermal mass are in constant natural convection to ambient temperature. Since this chain of connections were all made of metal and have a high value of thermal conductivity, it was reasonable to conclude that, compare to the thermocouple, the FBG sensor experienced a larger thermal cycle. The thermal fluctuation consisted of large oscillatory heat flux outflow through the flatplate package.

5.2.2 Sensitivity to Force

Figure 5-5 shows the measurement of FBG's Peak 1 and Peak 2 response with respect to the axial load applied. All measurements were made with the thermal chamber's temperature set to $30 \pm 0.1°C$.

Both of the peaks exhibit extremely high level of linear correlation with force sensor. The sensitivity values for each FBG peaks are,

$$\frac{d\lambda_1}{dF} = 0.104 \pm 0.000252\, nm/N$$

$$\frac{d\lambda_2}{dF} = 1.326 \pm 0.001780\, nm/N$$

With the coating, the force sensitivity is attenuated by almost 13 times compared to the bare fiber section.

Using a diameter of 125 μm and Young's modulus of 72 GPa, a bare fiber has an axial strain sensitivity in the range of 1130 $\mu Strain/N$. For the bare fiber section of the FBG, the strain sensitivity can be calculated as 1.17 $pm/\mu Strain$, which is very close to the value reported in literature, 1.20 $pm/\mu Strain$ [24], [68].

At higher temperature, as the FBG is heated up, the fiber elongates due to the thermal expansion of the material. The elongation adds to the existing mechanical strain due to the axial load. Hence a load reduction can be expected as temperature is increased. To ensure the FBG sensor always operate under tensile loading, a pre-tension is applied to the sensor by prescribing an initial amount of displacement, which is equivalent to 0.8 N of applied force at 30°C.

Figure 5-6 shows the temperature dependence of the Peak 2 wavelength to force sensitivity. Evidently, an increase in temperature produces an equivalent leftward shift to the Peak 2 response. At different temperatures, the force sensitivity is consistent as the curves are in parallel.

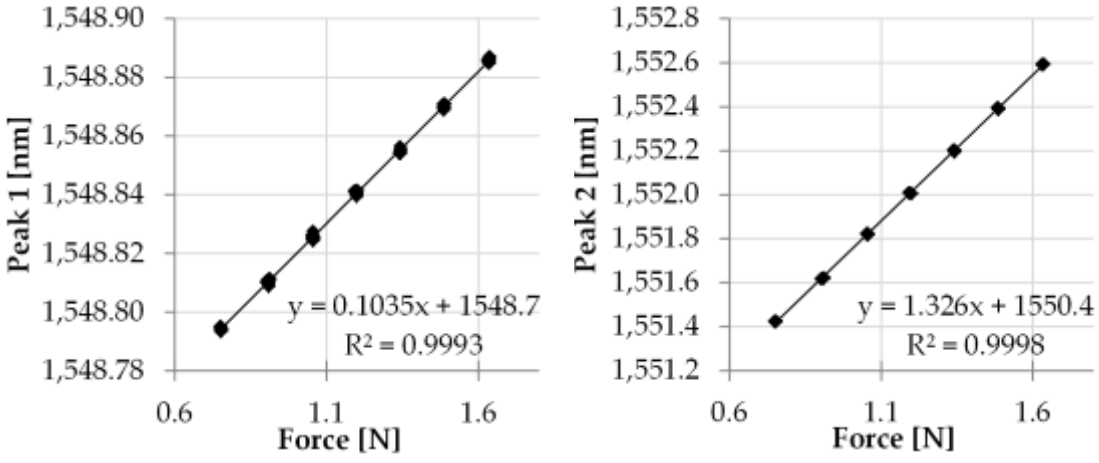

a) b)

Figure 5-5 Optical response of a) Peak 1 b) Peak 2 related to force.

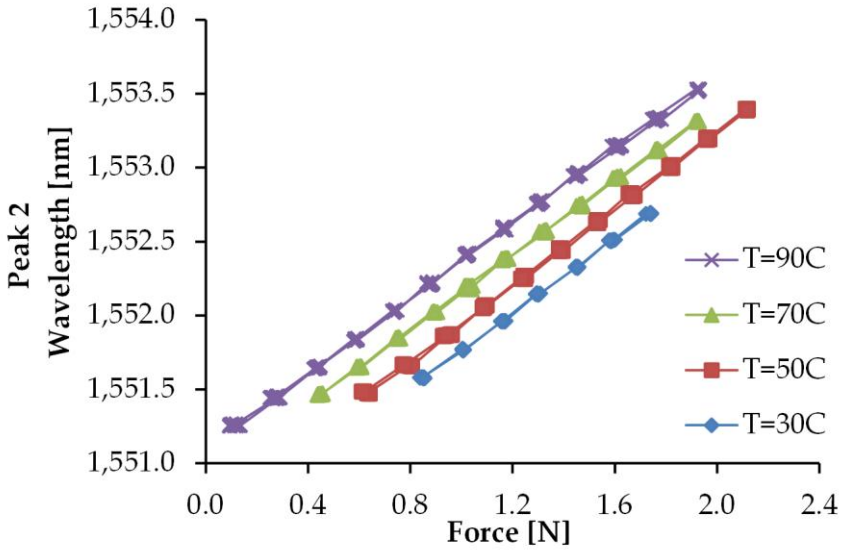

Figure 5-6 Temperature dependence of force measurement.

5.2.3 Calibration Matrix

Combining the effects of both temperature and axial loading, a multi-variable linear regression model was computed. For the sake of steady state measurement due to equipment limitation, the model aggregated only the steady state responses. The optical spectrum response is correlated to the change in referenced force measurement and temperature measurement.

$$\begin{bmatrix}\Delta\lambda_1\\ \Delta\lambda_2\end{bmatrix} = \begin{bmatrix}0.1031 & 0.0269\\ 1.2597 & 0.0108\end{bmatrix}\begin{bmatrix}\Delta F\\ \Delta T\end{bmatrix} \tag{5.1}$$

The coefficient of determination R^2 is 0.998 for $\Delta\lambda_1$ and 0.996 for $\Delta\lambda_2$, which shows an excellent linear fit.

Inverting the sensitivity matrix and we obtain the calibration matrix,

$$\begin{bmatrix}\Delta F\\ \Delta T\end{bmatrix} = \begin{bmatrix}-0.329 & 0.8178\\ 38.417 & -3.175\end{bmatrix}\begin{bmatrix}\Delta\lambda_1\\ \Delta\lambda_2\end{bmatrix} \tag{5.2}$$

The standard error of the calibration matrix is

$$\sigma_{\text{calib}} = \begin{bmatrix} 0.00122 & 0.0010 \\ 0.03219 & 0.0276 \end{bmatrix} \tag{5.3}$$

5.2.4 Verification

Using the calibration matrix from equation (5.2), the performance of the FBG sensor can then be benchmarked against the reference force and temperature measurements.

Figure 5-7 shows the steady state response of the FBG sensor, comparing the reference temperature measurement with the model using the calibration matrix. Again, the reference temperature measurement showed high oscillatory noise at high temperature due to calibration setup limitation as discussed in 5.1.

A number of force cycles were completed at different temperature set points. Each bidirectional force cycle was completed individually. Each of the force cycle response and its corresponding predicted value based on the linear model was piecewise merged as shown in Figure 5-8. The figure shows two thermal cycles, each thermal cycle has a step of 20°C. Overall, the model prediction showed excellent agreement with the experiment result. However, there was a tendency of a larger mismatch, at lower temperature (30°C), at the start of the second thermal cycle.

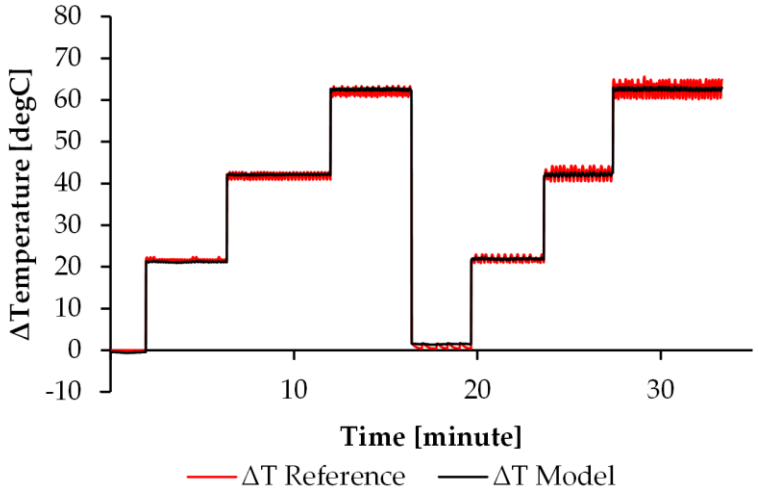

Figure 5-7 Steady state temperature response at different temperature set point: reference vs model.

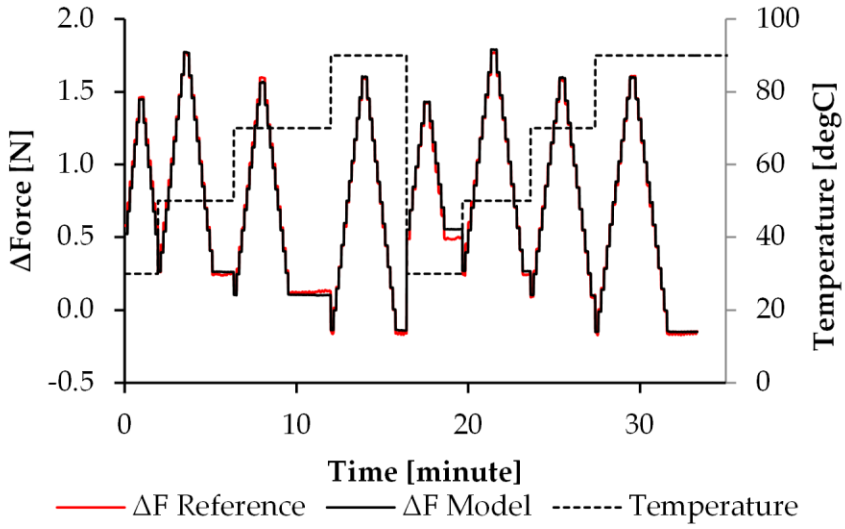

Figure 5-8 Force response at different temperature set points: reference vs model.

After each thermal and force cycle, the overall optical response was observed to be shifted slightly. The drift at low temperature could be attributed to the creep in the epoxy. This effect was especially evident for the initial thermal cycles but tended to vanish at high cycle count, as further discussed in the next section.

From this experiment, the full-scale tensile force applied totaled to 1.94N. The discrepancy seen at low temperature was calculated to be $\pm 3.25\%\ FS$. This value also corresponded to the global maximum error.

5.3 Repeatability

For reliable operation, the repeatability of the sensor is an important performance parameter to be investigated. The following sections analyze the stability performance of the epoxy after several thermal and tensile loading cycles.

5.3.1 Temperature

For the analysis to follow in this section, same temperature and tensile loading conditions were applied to the sensor on different days. Peak 1 was first analyzed at low and high temperature set points. A total of four temperature cycles were conducted in the following sequence.

Table 5-1 Thermal cycle sequence

Cycle #	Temperature Set Point Sequence (°C)
1	30 - 50 - 70 – 90
2	30 - 50 - 70 – 90
3	30 - 50 - 70 - 90
4	30 - 50 - 70

Each of the thermal cycle started at ambient temperature and ended with cooling to ambient temperature. Each individual cycle was completed with one day apart. Multiple tensile loading cycles were applied during each step of thermal cycle steps.

Each data point shown is an average of at least 30 samples taken at 5 seconds interval after the steady state temperature is reached. Figure 5-9a shows the measurement of Peak 1 at low temperature while Figure 5-9b shows the measurement at high temperature. At 30°C, Peak 1 response converged to roughly $1548.87 \pm 0.000554\ nm$, after three thermal cycles. At 90°C, Peak 1 also settled to $1550.405 \pm 0.00194\ nm$. As for the long term drift for peak 1, there was a total of $+87\ pm$ drift at 30°C and a drift of $-20\ pm$ at 90°C.

Evidently, there is a much higher spread in Peak 1 at high temperature, which is consistent with the result obtained in earlier analysis. The standard deviation in each sample set is plotted as bar chart in Figure 5-10. The maximum standard deviation did not exceed 9 pm, which could be attributed to the measurement error from the optical interrogator. The optical interrogator has an accuracy specification of 10 pm [69].

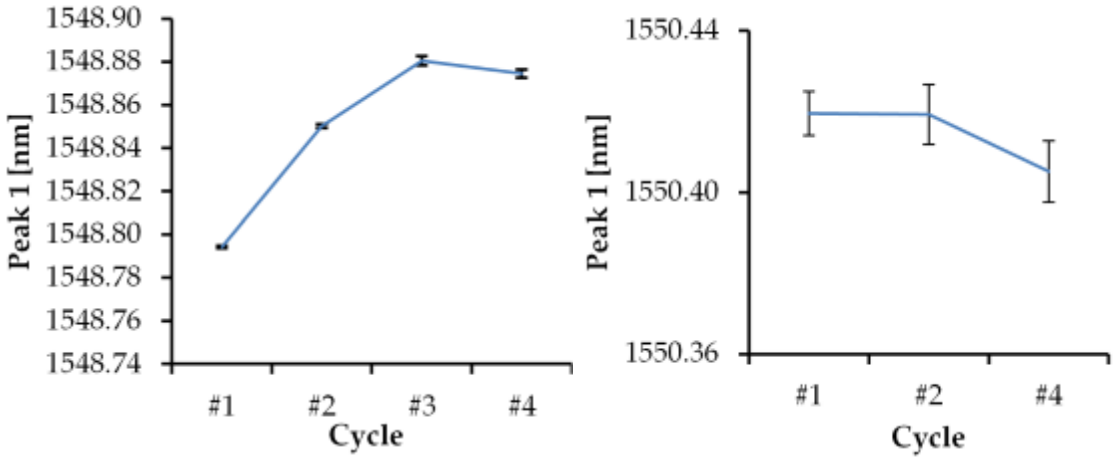

Figure 5-9 Average of Peak 1 at zero load: reference vs each tensile load cycle at a) 30°C b) 90°C.

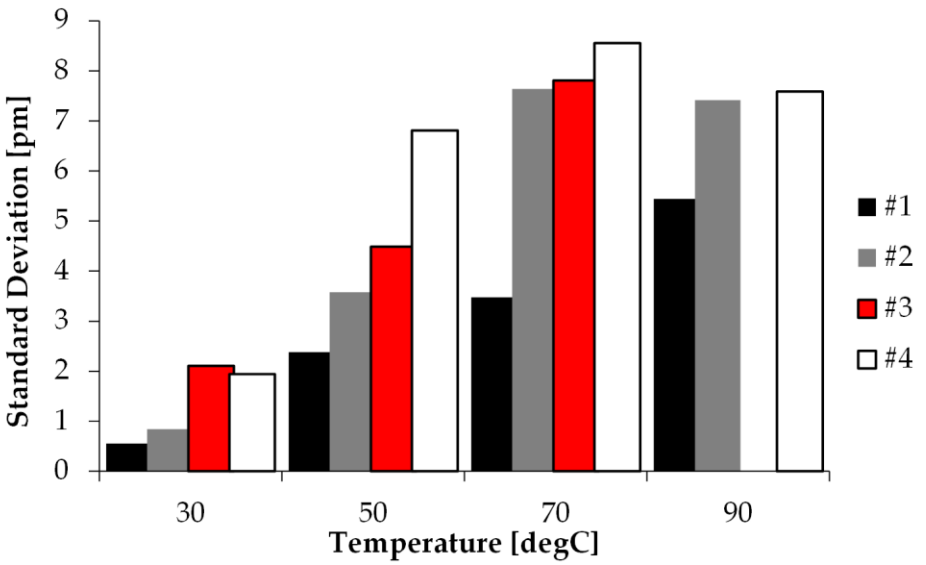

Figure 5-10 Standard Deviation of Peak 1 at zero load reference (legend: thermal cycle).

A similar trend was observed for Peak 2 at both low and high temperature experiments, as seen in Figure 5-11.

In Figure 5-12, across the temperature range from 30-90°C, show the maximum standard deviation in the sample is approximately 4 pm, which is only half of the one seen in Peak 1.

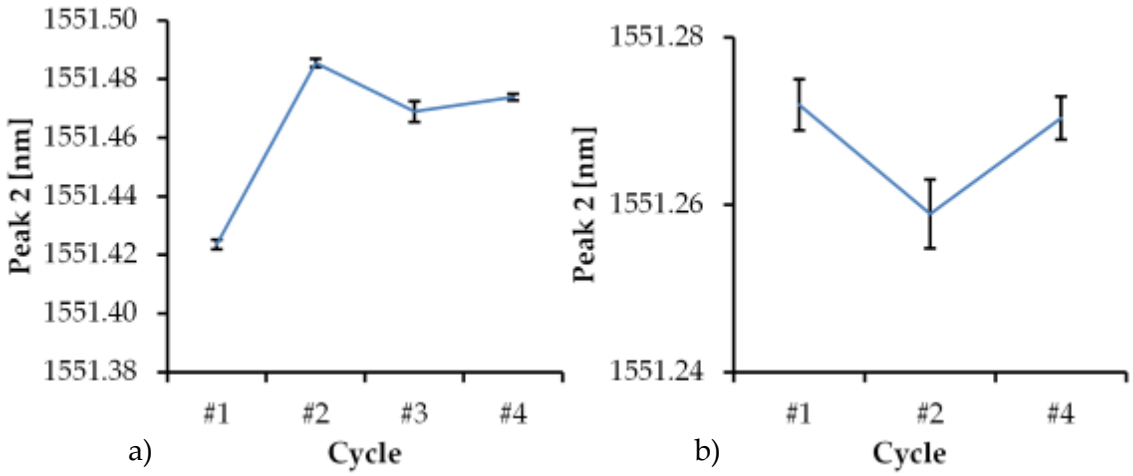

Figure 5-11 Average of Peak 2 at zero load: reference vs each tensile load cycle at a) 30°C b) 90°C.

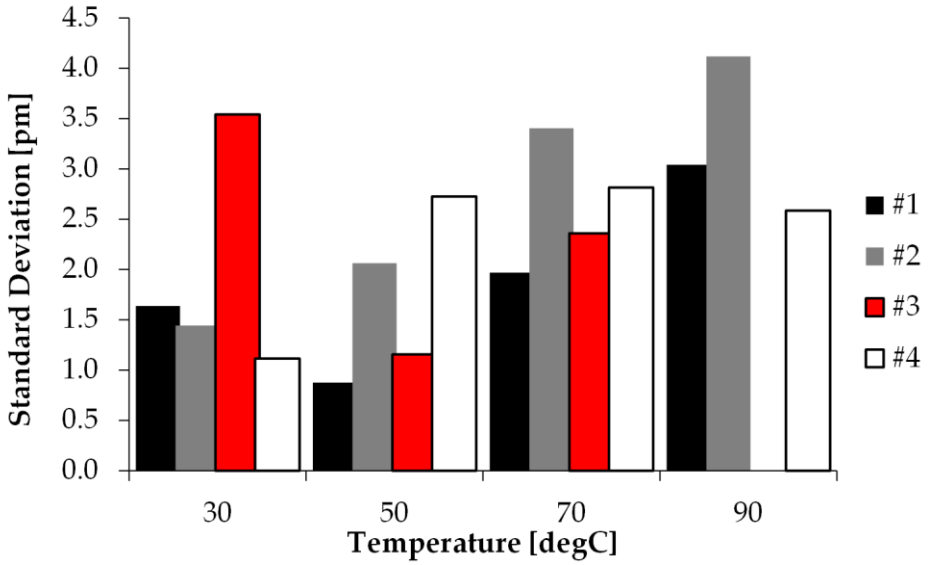

Figure 5-12 Standard deviation of Peak 2 at zero load reference (legend: thermal loading cycle).

5.3.2 Strain

For the case of strain loading - two extremes were also presented here: high and low displacement/strain at high and low temperature. At each of the temperature set point, the sensor had undergone at least 15 displacement controlled bidirectional tensile loading/unloading cycles. At each of the cycle,

1 Displacement (Δd) increment at step of 5 μm, from 0 to 30 μm, then return from 30 to 0 μm

2 Position was held at each location for 10 seconds

3 Data was collected at 1 second interval.

4 Each data point, shown in the following charts, represented the average of 6 measurements, while the error bar represents the standard deviation.

Low Temperature: 30°C

Setting: $\Delta d = 0\ \mu m$

Unlike the steady state comparison for thermal cycles, tensile cycles resulted in an overall downward trend in wavelength measurement. Figure 5-13 shows Peak 2 has a maximum drift of $-20 pm$ after 15 tensile cycles. However, the response seemed to settle to $1551.483 \pm 0.001\ nm$.

Setting: $\Delta d = 30\ \mu m$ or equivalent $\Delta Strain_{bare} \cong 1052\ \mu m/m$

At higher tensile loading, Figure 5-14 shows that Peak 2 exhibited a downward drift of $-15\ pm$ after 16 tensile loading cycles. However, the measurement seemed to have a higher fluctuation and the downward drift seemed to continue even after 16 tensile cycles. This was still acceptable as the majority of the measurements fall under a $10\ pm$ wide band between $1552.600\ nm$ and $1552.590\ pm$.

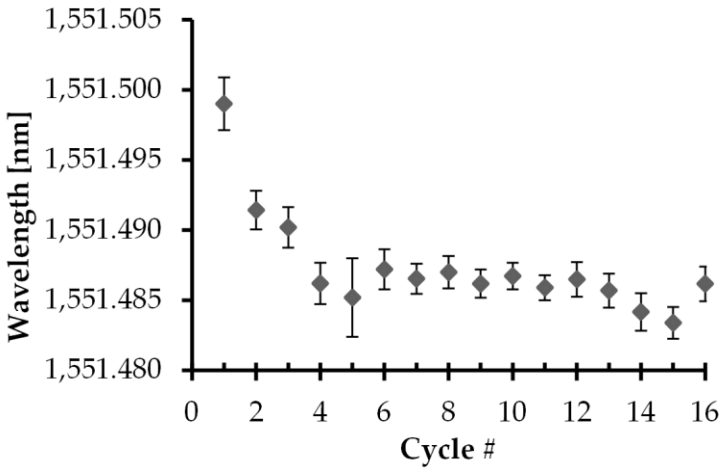

Figure 5-13 Peak 2 response of zero displacement at each tensile cycle.

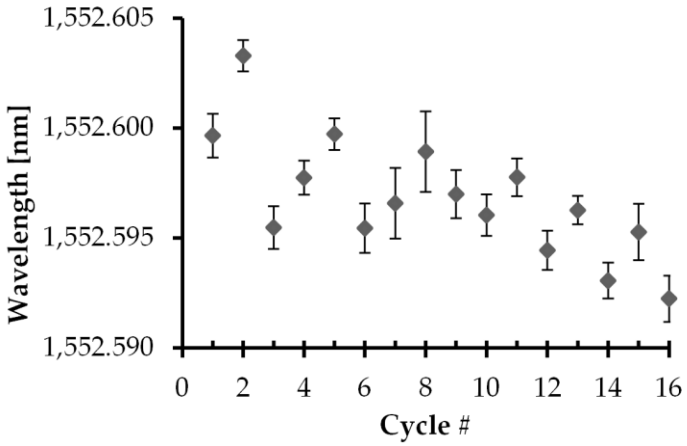

Figure 5-14 Peak 2 response of 30 μm displacement at each tensile cycle.

High Temperature: 90°C

Setting: $\Delta d = 0\ \mu m$

At high temperature and zero displacement, a downward oscillatory trend was evident from Figure 5-15. It had a maximum drift of $-40pm$ and it seemed to settle to $1551.259 \pm 0.003\ nm$.

Setting: $\Delta d = 60\ \mu m$ or equivalent $\Delta Strain_{bare} \cong 1987\ \mu m/m$

Similar downward drift amplitude was observed for high temperature and high displacement. The maximum drift was $-35pm$. After the 7th cycle, subsequent Peak 2 measurements seemed to be abruptly shifted up by 20 pm, deviating from the expected trend shown before cycle 7.

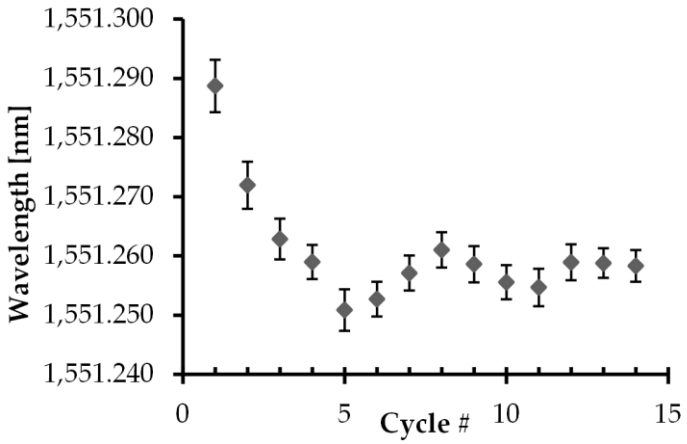

Figure 5-15 Peak 2 response of 0 μm displacement at each tensile cycle.

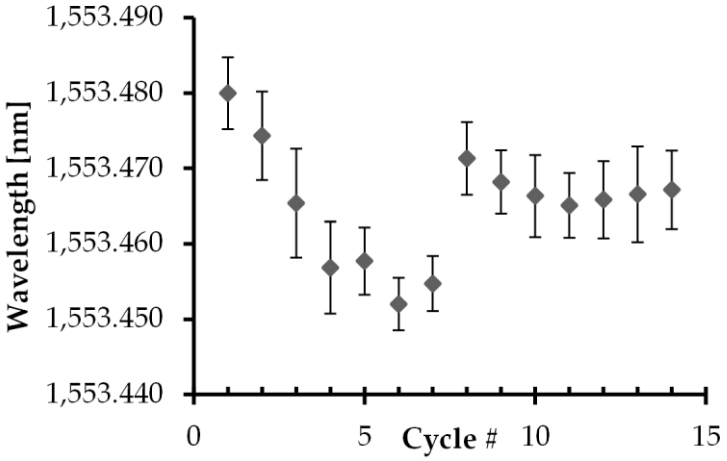

Figure 5-16 Peak 2 response of 60 μm displacement at each tensile cycle.

It is unknown the exact cause of this shift. It should be safe to discount the significance of this shift as this trend is not evident in any other measurements. Likely cause of this shift can be a small unintended vibration to the calibration setup or a sudden measurement error from the equipment.

5.4 Summary

A previously developed fiber optic calibration setup was employed for the characterization of the coated FBG. The limitation and dynamics of the setup was then documented, analyzed, and discussed. The FBG sensor design was then fully characterized using the calibration setup, while minimizing measurement error given the limitations. A multi-parameter linear regression model was used to characterize the sensor to both temperature and axial force loading. A highly linear response of the FBG sensor was observed. The coated section of the FBG exhibited a 2.7 times increase in sensitivity to temperature while the force sensitivity was attenuated by 13 times. Finally, the reliability of the sensor was investigated. Experimental measurement showed both peaks of the FBG experiences drift but the drift tended to settle after 3 thermal cycle loading, and after 5 – 10 tensile loading cycles.

6 High Pressure Packaging

The goal of this chapter is to present and investigate a high pressure package design for applications in areas such as the oil well down-hole monitoring. The nature of a harsh and corrosive environment in the oil and gas industry requires a robust packaging strategy to ensure a reliable and uninterrupted operation.

As investigated in the literature, most high pressure FBG sensor designs rely on cantilever beams or diaphragms to measure the deflection of the fiber [6], [7]. This type of design has the challenge in assembly and further miniaturization as the intricate cantilever beam or diaphragm can be easily damaged during the assembly or fabrication process. To achieve multi-parameter sensing, additional FBGs need to be bundled in the package. This increases the complexity of the packaging further. Another popular design found in many patents for multi-parameter harsh environment sensing involves the use large stainless steel tubes to protect the FBG sensors [6], [18], [50], [51]. All the designs involve the use of at least one additional FBG for temperature compensation on a fixed thermal reference body. This type of design again increases the complexity and makes the package bulky to account for multiple pieces for assembly.

The packaging design investigated here is to accommodate the FBG coating technique for simultaneous multi-parameter measurement as presented in the previous chapters. The design study starts with a pilot study of a concept design.

6.1 Design Specification

The design task for the coated FBG package should address the challenges currently present as discussed from the literature review. The design must complement the dual parameter sensing capability of the coated FBG as presented in Chapter 3. Specifically, the design specifications are the following:

- Minimized profile - entire package must be fitted in a ¼" stainless steel pipe
- Maximum pressure rating - 3000 psi (20.68 MPa)

- Target mechanical response - 1000 μStrain axially applied on fiber optic
- Design must allow easy integration for multiplexed distributed sensing in a serial fashion

6.2 Initial Design

This section presents an axial symmetric packaging design that directly converts pressure into axial strain on the fiber. The shape of the proposed design resembles the shape of a dumbbell. Due to the axial symmetry, multiple sensors can easily be daisy-chained together for distributed sensing application.

Figure 6-1 shows the conceptual design of the proposed package in 2D cross sectional view. The design exposes the middle part of the package to external pressure. There are three separate parts in this design,

- Two end caps (with center hole for fiber to pass through)
- Sleeve (hollow tube)
- Fiber

The arrows in Figure 6-1 indicate the applied hydrostatic pressure. The end cap on the right is fixed while the one on the left is freed to move linearly in the axial direction. The sleeve acts as a protective cover as well as a mechanism to attenuate the overall strain imposed on the fiber.

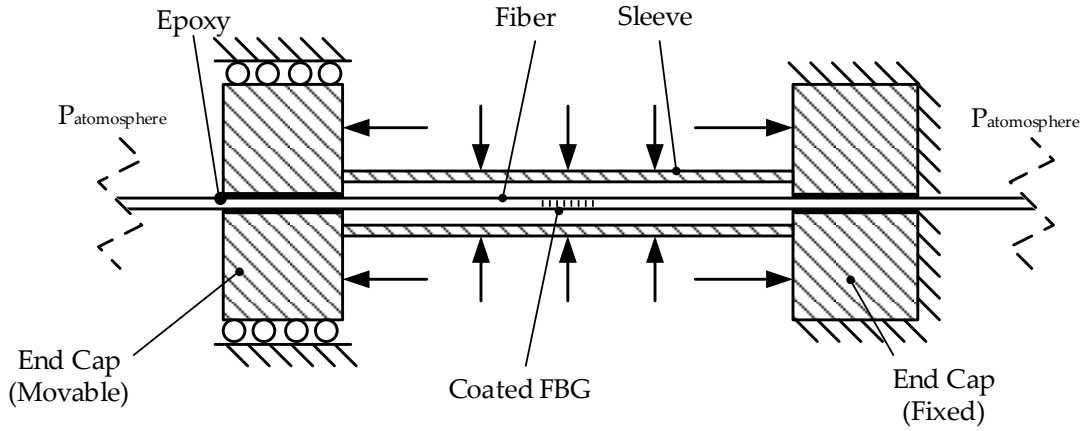

Figure 6-1 Schematic of concept design of high pressure package.

By careful design of the material in the sleeve and the thickness of the sleeve, one can optimize the sensor performance of the FBG.

6.3 Detailed Design

After the initial pass of finite element analysis of the package, the detailed design phase is required to convert the concept study into a practical design, appropriate for lab testing. Several mechanical aspects of the design are considered at this stage:

- **Sealing under high pressure**: an o-ring groove is added to provide a practical implementation of creating a seal in the pressure senor package,
- **Manufacturability**: the sleeve at the centre of the package is designed so it can be purchased off the shelf as a hollow tube; length of the caps are extended for ease of machining,
- **Machining tolerances**: dimensional tolerances are added,
- **Assembly**: Grooves are designed with appropriate depth to mate with the sleeve,
- **Durability**: chamfers are added to all sharp corners to reduce stress.

Figure 6-2 shows a CAD model cross section of the sensor package. The two end cap pieces are expected to be bonded to the centre sleeve by epoxy. Invar 36 alloy is chosen as the material main body of the package, due to its exceptional low thermal expansion coefficient (the lowest in any metal alloy $-1.2 \times 10^{-6}\, 1/°C$) while having a high mechanical strength.

A number of o-ring materials were investigated. Final design selection is to use Perfluorinated Fluoroelastomer, which carries the commercial name Viton. Viton is the ideal candidate as this elastomer has a proven track record for harsh environment applications in the oil and gas industry.

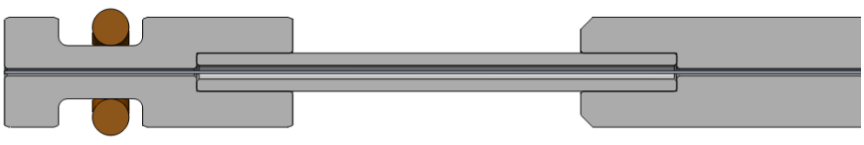

Figure 6-2 Detailed design CAD model of high pressure package.

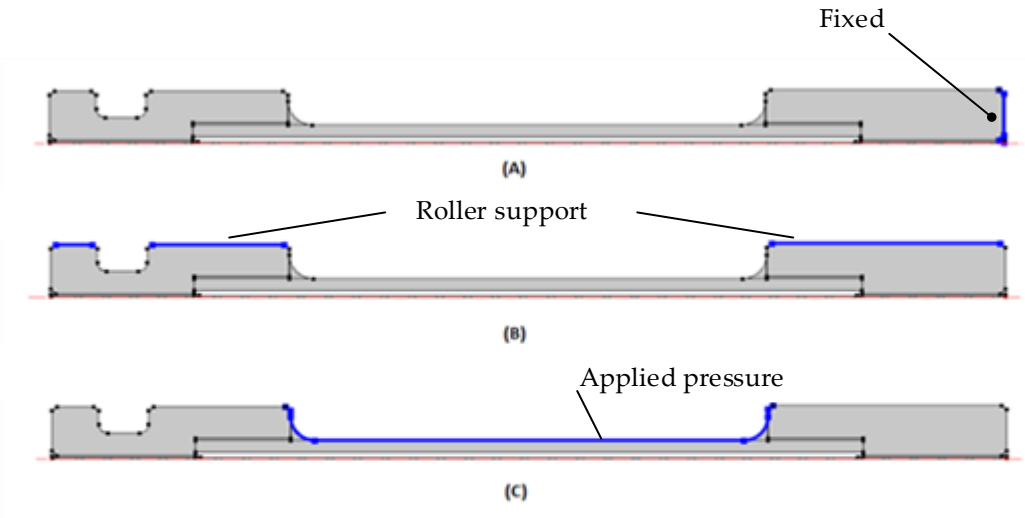

Figure 6-3 FEM model boundary conditions.

It has exceptional resistance to chemical, temperature, and oil for environments with extreme temperature. It has an operating temperature of up to 320°C [70].

6.3.1 Finite Element Analysis

To further analyze the mechanical performance of the package and to optimize the geometric parameters, an FEM model is developed in COMSOL Multiphysics®.

The axial symmetric nature of the package is leveraged in the FEM model to minimize computational time required. Figure 6-3 shows the application of the boundary conditions.

6.3.2 Mesh Independency

Using the refine mesh function in COMSOL, the mesh can be refined without remapping the meshes. This is achieved by subdividing each triangular mesh element into four smaller triangles. Figure 6-4 shows the mesh refinement at two different steps. The refinement is applied to both the sleeve domain and the epoxy domain as they are the expect area of high stress concentration.

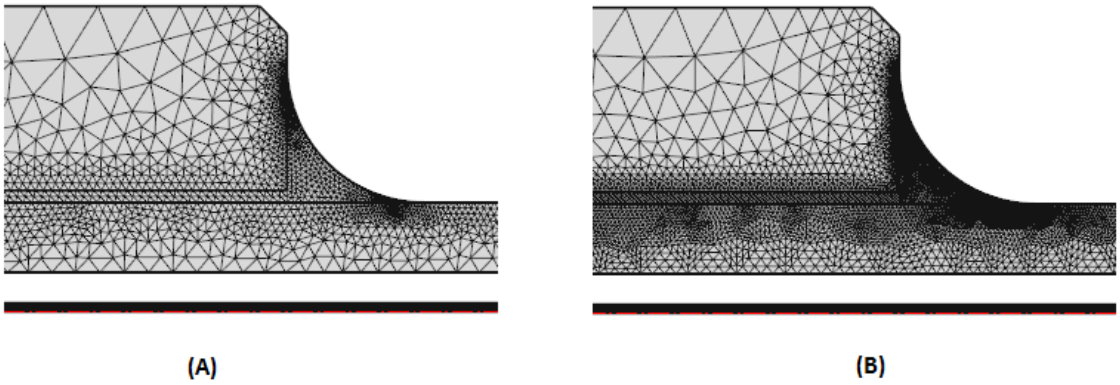

Figure 6-4 Mesh refinement at a) step = 1 b) step=3.

Figure 6-5 shows the maximum global Von Mises stress and maximum strain in correlation to the number of refinement steps. Evidently, steady state was reached after three steps of refinement. This shows the numerical solution is stable and converges. Three steps of refinement, corresponding to 96,090 mesh elements, was therefore used for subsequent FEM analysis.

6.3.3 Effect of Sleeve Thickness

The thickness of the sleeve is the key parameter for the overall elongation of the package, which is translated into imposed strain on to the coated FBG body.

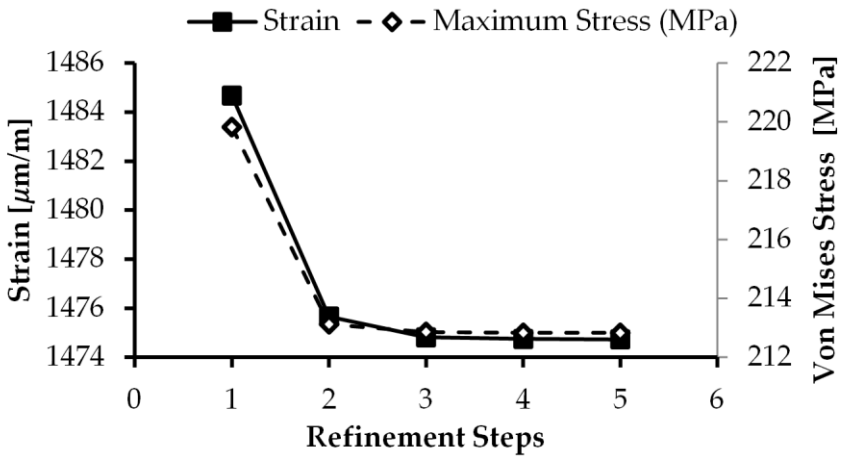

Figure 6-5 Mesh independency for the detailed design.

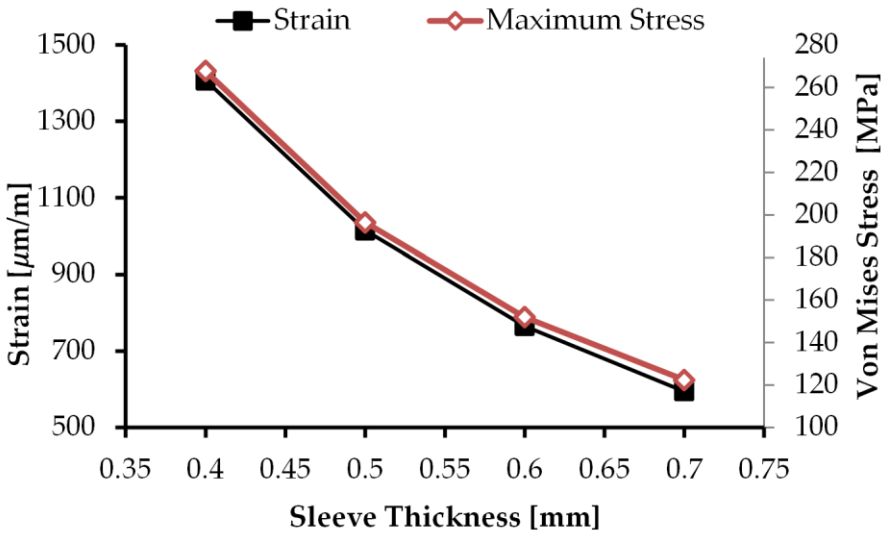

Figure 6-6 Computed strain and maximum von mises stress vs sleeve thickness.

A parametric sweep study was performed on the sleeve thickness. Sleeve thickness was swept from 0.4 mm to 0.7 mm with a step of 0.1 mm. Figure 6-6 shows the correlation between maximum global Von Mises stress and average axial strain at the centre of the FBG fiber.

The correlation between sleeve thickness to both stress and strain can be accurately modelled with a second order polynomial. This relationship was expected as the sleeve diameter relates to the cross sectional area in the 2nd order nature.

The maximum stress occurs at the sleeve. Since Invar 36 was the material selected for the sleeve, the maximum Von Mises stress should not exceed the yield strength of the material to ensure there was no plastic deformation in the package. Invar 36 has a yield strength of 276 MPa [71].

The design goal is was maximize strain while minimizing the maximum Von Mises stress. Hence a new ratio can be introduced to evaluate the significance of both strain and stress.

$$Ratio = \frac{Strain}{Stress}$$

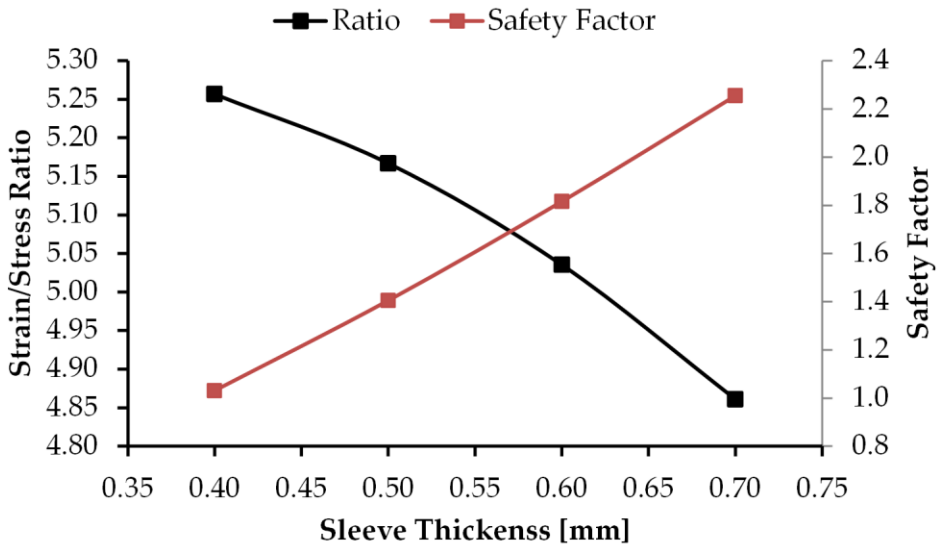

Figure 6-7 Strain/Stress ratio and safety factor vs sleeve thickness.

The mechanical design safety factor can also be calculated and is plotted in Figure 6-7. For safety, any design with a safety factor < 1.2 must be rejected. Hence any sleeve thickness from 0.5 mm to 0.7 mm was acceptable. For the final design, 0.5 mm was selected to be the optimized thickness dimension.

6.4 Final Design

After several design iterations, the final mechanical design revolved into an unibody design, as the schematic shown in Figure 6-8. An additional groove was added to accommodate a secondary o-ring for safety. Two grooves were added on two ends of the package for adapter as the fiber grabber for ease of assembly.

6.5 Experiment Methods

To evaluation the performance of the designed package, a safe and reliable test rig must be designed to deliver high fluid pressure to a controlled region (centre of the sleeve) of the package.

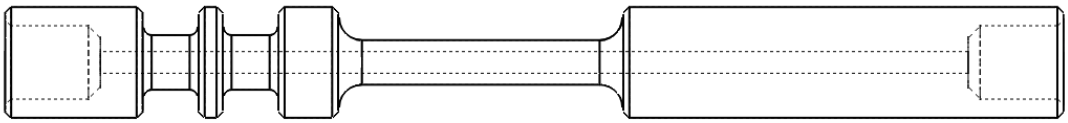

Figure 6-8 Final mechanical design.

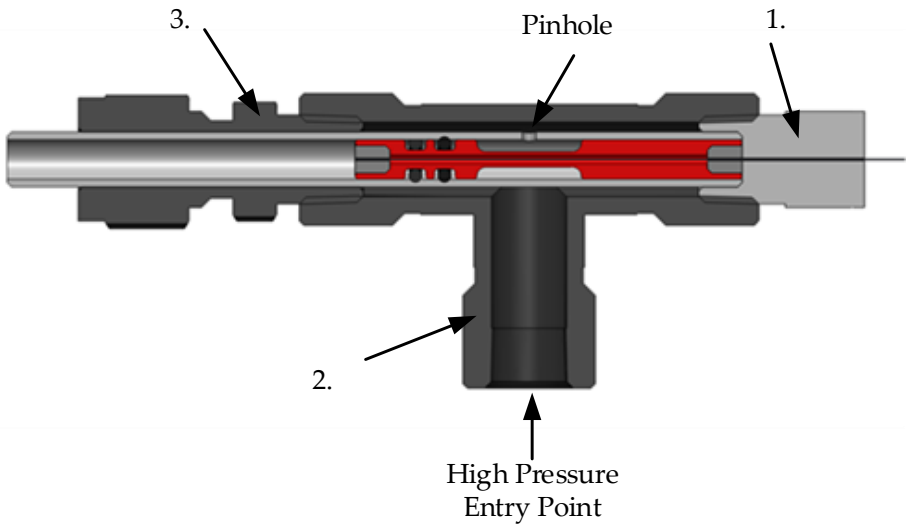

Figure 6-9 Cross sectional view of the test rig package.

The design of the test rig involved the use of multiple off-the-shelf pipe fitting components to seal the package from potential leakages. Some of the parts were modified mechanically to suit the specific need in this configuration. These parts are listed below and also illustrated in Figure 6-9.

1. Swagelok 1/8″ NPT pipe plug
2. Swagelok 1/8″ NPT Female Tee Joint
3. Swagelok 1/8″ NPT to 1/4″ Straight Fitting

High pressure fluid is expected to enter the T joint and fill the cavity around the sleeve of the FBG package via the pinhole. The fluid was sealed by the modified straight fitting on the left, as well as the pipe plug on the right. The material for all pipe fittings were selected to be Stainless Steel 316 which has a pressure rating of 20 kpsi [72], well over the maximum pressure of 3000 psi to be applied to the sensor package.

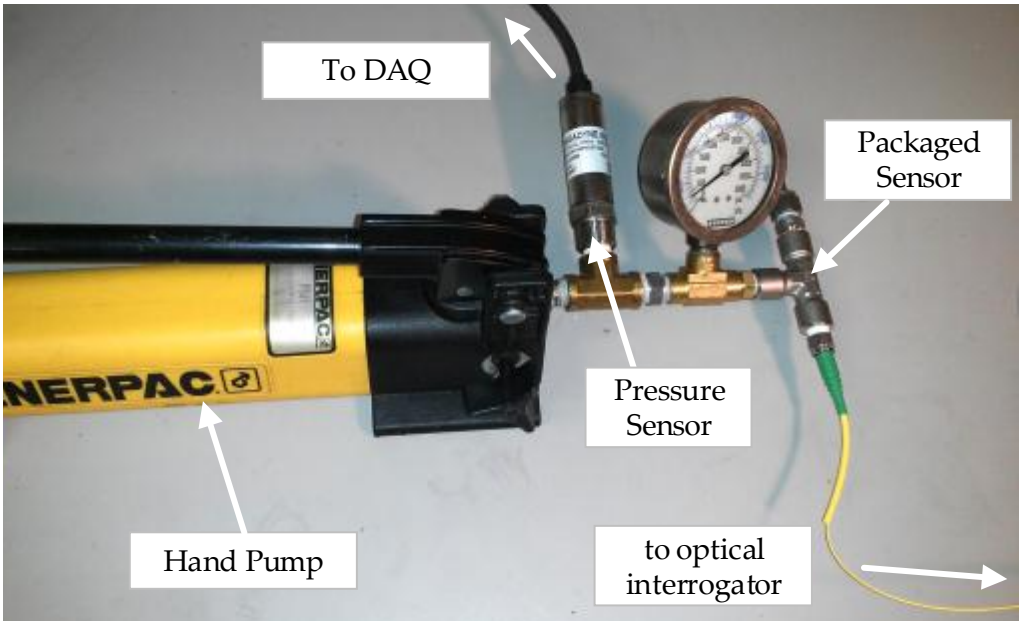

Figure 6-10 Test rig setup.

6.5.1 Setup

Figure 6-10 shows the physical setup of the test rig after all components were assembled. An Enerpac hand pump was used to provide incremental pressure to the packaged sensor. An electrical pressure sensor was attached via a tee joint to provide reference measurement.

Table 6-1 Equipment for testing the design package

Equipment	Model	Accuracy
Hand Pump	Enerpac P-141	N/A
Pressure Sensor	OMEGA MMG3.5KV5P4C0T3A5	± 7 psi
Thermocouple Reader	NI USB 9211	1 μV
Thermocouple	OMEGA Type T	0.04 °C
Hotplate	Thermo Scientific HP131225Q	N/A
DAQ	NI USB 6009	N/A
Optical Interrogator	Micron Optic sm125-200	10 pm

A hotplate and a thermocouple, not shown in the figure, were used to provide thermal loading and reference reading respectively. Table 6-1 shows the complete list of the equipment used to validate the high pressure package design.

6.6 Results and Analysis

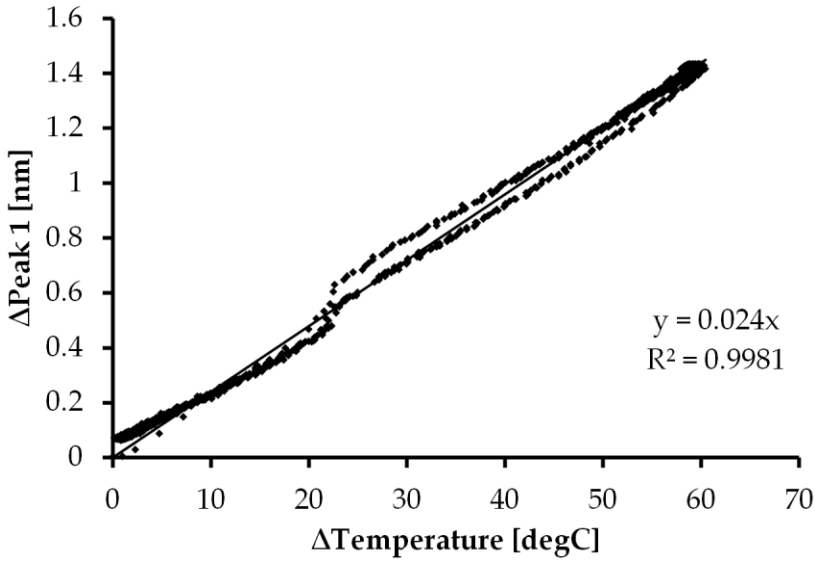

Figure 6-11 Temperature sensitivity of the packaged FBG.

Figure 6-11 shows that the response of the packaged FBG has a linear response to the change in temperature. The sensitivity of the package FBG was 23.96 $pm/°C$, which was slightly lower compared to the sensitivity from the flatplate package - 26.90 $pm/°C$.

After the first thermal cycle, a drift of 69.4 pm was observed at initial temperature reference. This is in excellent agreement with the drift seen from the flatplate package, which had a $+70\ pm$ drift after the 2nd thermal cycles. Compared to the FBG on the flatplate package, the temperature response of the packaged FBG had a small amount of hysteresis.

Figure 6-12a shows the sensitivity of packaged FBG Peak 2 to the pressure applied at $30°C$. The relationship could be well fitted with a second order curve. This showed that at low pressure, the package had a lower sensitivity value compared to the ones at higher pressure.

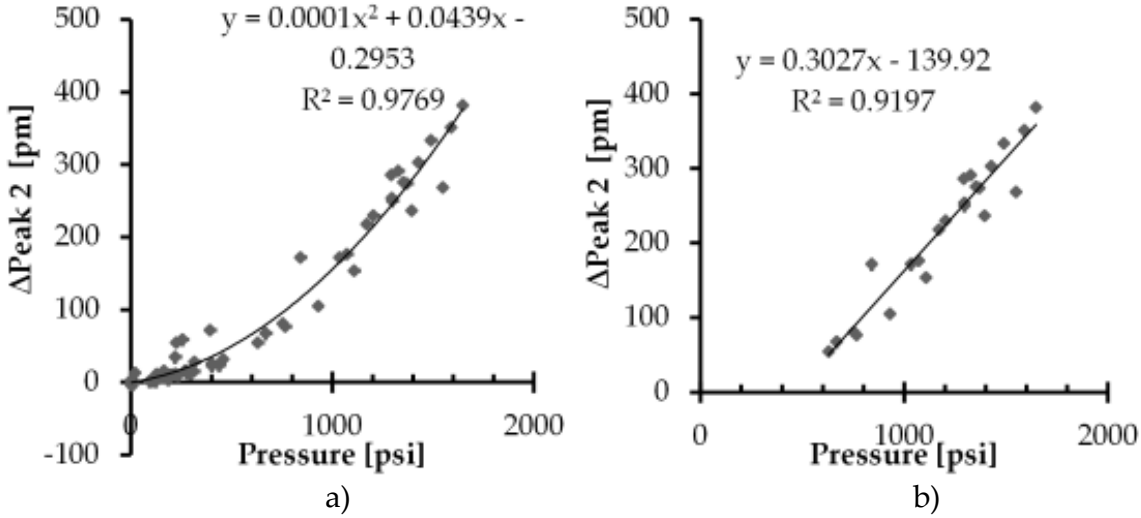

Figure 6-12 Pressure sensitivity of the FBG with a) all measurement and b) high pressure only.

This could be attributed to the lack of pre-tension in the fiber and the effect of the O-ring used in the package. There existed small movements and deformation of the O-ring at low pressure that resulted in a lower sensitivity response to applied pressure. Once the initial resistance was overcome, the response at higher pressure exhibited more of a linear response.

Figure 6-12b shows a relatively good match of linear response if we only consider the pressure higher than 600 psi. This results in a pressure sensitivity of 0.303 pm/psi. As a sanity check from the FEM model, the pressure sensitivity was predicted to be 0.396 pm/psi given a pressure of 3000 psi induces 1015 $\mu Strain$ and the sensitivity of bare fiber was 1.17 $pm/\mu Strain$. The slightly lower pressure sensitivity reported here can be attributed to error in modelling constants of the materials, as well as the dimensional uncertainties in the thickness of the sleeve, which was the key determining factor for the pressure sensitivity. Figure 6-13 shows the upward path and downward path of the Peak 2 response.

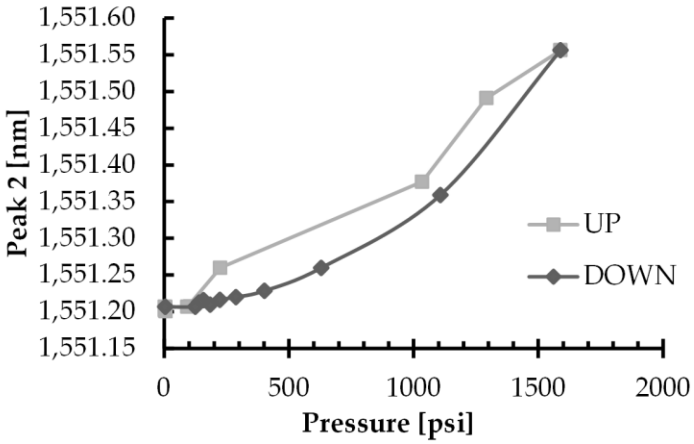

Figure 6-13 Hysteresis effect in the packaged FBG.

Both paths follow the second order trend. The hysteresis effect can be attributed to both the increased of epoxy in the packaged FBG and the lack of pre-tension in the fiber. During the assembly and the bonding process of the coated FBG, the suspended section of the FBG in the package can lose tension. This loss of tension was caused by the higher thermal expansion of the package, as the epoxy is thermally cured to 150°C and cooled to the ambient temperature. The loss of tension of the FBG was encapsulated in the mechanical package which resulted in the hysteresis effect and non-linear behavior in the strain response of the FBG.

Using the same characterization method of multi variable linear regression, a similar sensitivity matrix is obtained as the following,

$$\begin{bmatrix}\Delta P\\ \Delta T\end{bmatrix} = \begin{bmatrix}-85.61 & 5017.59\\ 41.21 & -5.87\end{bmatrix}\begin{bmatrix}\Delta\lambda_1\\ \Delta\lambda_2\end{bmatrix} \tag{6.1}$$

The regression model for ΔT has R^2 =0.9996 which warranted a curve fit with good approximation. ΔP has a much lower R^2 value - 0.9345. This was anticipated due to the non-linear effects as discussed earlier.

6.7 Summary

This chapter presented a package design for the application in high pressure measurement in harsh environment. A concept study was first presented with a follow up of a detailed study. A finite element model was developed for the detailed design to assist the optimization of the sleeve thickness parameter. The experimental method was then presented to characterize the performance of the package with a coated FBG. The experimental result showed excellent agreement of both temperature and pressure sensitivity when compared with the results obtained from the flatplate package.

7 Conclusions

The following conclusions can be drawn from this thesis:

- ***A novel fiber coating process is developed using a gauge 30 needle and a two component thermal curing epoxy***

  Dual parameter discrimination is achieved by covering half of the FBG length by using a metallic insert.

- ***An opto-mechanical FEM is developed and linked to an optical model based on couple mode theory.***

  The opt-mechanical model is validated by the accurate prediction of optical response for both thermal and axial loading cases. Discrepancy starts to occur at $T = 90°C$ as the epoxy starts to enter the glass transition temperature range and experience a reduction of Young's modulus and increase of CTE.

- ***Sensitivity of the FBG with half coated metal insert can be fully characterized and calibrated***

  Coated FBG has 2.7 times higher temperature sensitivity than bare fiber, while coated FBG has 13 times lower force sensitivity than bare fiber. A multi-parameter linear regression model is used to derive a calibration matrix. The prediction of force and temperature is in close agreement with subsequent experimental as validation

- ***Creep causes drift in the FBG optical response but it tends to settle after several loading cycles***

  High amount of drift for both Peak 1 ($+70\ pm$) and Peak 2 ($+25\ pm$) is observed at low temperature (30°C) but the drift settles after the 3rd thermal cycle. Under tensile loading cycle, Peak 2 has a maximum drift of $-40\ pm$ but settles to within $\pm\ 5\ pm$ after 7 loading cycles

- ***A design for high pressure FBG sensor is proposed and optimized using FEM study***

The optimal design is using a sleeve thickness is 0.5 mm, which induces 1015 μm/m of axial strain on the fiber while it has a Safety Factor of 1.4. The geometry involves a dumbbell design where the coated FBG can be encapsulated within.

- ***High pressure sensor prototype shows a linear response with temperature while response with pressure is a second order one.***

  The temperature sensitivity is 23.96 $pm/°C$, about 10% lower compared to the flatplate packaged, which is 26.9 $pm/°C$. At pressure higher than 600 psi, the pressure sensitivity can be better modelled as a linear response with sensitivity of 0.303 pm/psi, in close agreement with the FEM model sensitivity prediction -0.390 pm/psi. The nonlinear response of the pressure package at low pressure can be mostly attributed to the lack of pre-tension on the fiber, which introduces hysteresis and the lower pressure sensitivity. Therefore, the application of pre-tension on fiber prior and during the thermal cure process for epoxy is critical for accurate and reliable performance in low pressure.

8 Future Work

As a result of the design analysis from this thesis, the following should be pursued as further investigation:

- ***A detailed analysis of the mechanical and thermal material property of the thermal curing epoxy should be studied in house***

  To increase modelling accuracy for high temperature operation, the performance parameters of the epoxy should be fully understood and characterized as limited information is provided by the supplier. These performance parameters include lap shear strength, glass transition temperature, CTE, creep, and hysteresis, as a function of temperature.

- ***The calibration station with thermal chamber should be redesigned for accurate high temperature control***

  It is recommended to directly attach a heating source to back of the flatplate package. Thermal insulating plates should also be used to minimize heat conduction to the mounting plates attached to two large thermal masses. The station should accommodate high temperature characterization of up to 300 °C for future needs.

- ***A real time peak measurement system should be developed***

  The data collection/analysis process can be further optimized by integrating the level crossing detection algorithm in the custom LabVIEW acquisition software.

- ***A mechanical rig should be designed to assist the assembly process of future sensor prototypes***

  The rig will be able to apply adjustable tension to the fiber, even during the thermal curing process for the epoxy. The rig should include a modular design that allows FBG to be mounted on any future package designs.

Appendix A – MATLAB Source Code

```
clf;
global lambda L fl1 e_com1 e_com2 dT  e_T alfa DT offset;

% ======================================
% ======================================
% Differential Equation Solver Driver %%%
% ======================================
% ======================================

alfa=0.55e-6;
L=10e-3;                              % Length of FBG;
Ref_M=[];
lambda_M=[];
lambda_centre = 1550e-9;
lambda_min=lambda_centre - 4e-9;
lambda_max=lambda_centre + 4e-9;
d_lambda=10*1e-12;                    % Wavelength Resolution
nu=0.16;                              % Poisson's Ratio
dT=0;
offset = 0.3e-3;
cFactor = 1;

other=[1];

%% Model Input
Temp=[];                              %     delta T

% Bare
s_set = [];
Strain1=[s_set(1)]*1e-6;
Strain1t=[s_set(2)]*1e-6;

% Covered
Strain2=[s_set(3)]*1e-6;
Strain2t=[s_set(4)]*1e-6;

n_other = length(other);
n_strain = length(Strain1);
peak = zeros(n_strain,1);
peak_w = zeros(n_strain,1);

Color=varycolor(n_strain*n_other);

for j=1:length(n_other)

    n_lmbd = length(lambda_min:d_lambda:lambda_max);
    Ref_M=zeros(n_strain,n_lmbd,n_other);
    lambda_M=zeros(n_strain,n_lmbd,n_other);

    for i=1:length(Strain1)
        %strain_T=Strain(i);
        DT=Temp(i);
        e_com1=[Strain1(i);Strain1t(i);Strain1t(i)];
```

```
        e_com2=[Strain2(i);Strain2t(i);Strain2t(i)];

        fl1=1;
        k = 1;

        for lambda=lambda_min:d_lambda:lambda_max;

            R=runge_kutta4_FBG(L/2,-L/2,400,0);
            z=R(:,1);
            ro=R(:,2);
            Ref_M(i,k,j) = abs(ro(end))^2;
            lambda_M(i,k,j) = lambda;

            k = k+1;
        end;

        Ref_M(i,:,j)=cFactor*Ref_M(i,:,j);

        pow = 10*log(Ref_M(i,:,j)');
        %pow(pow<-60)=-60;

        [v, ind] = max(pow);
        peak(i) = lambda_M(i,ind,j)*1e9;
        peak_w(i) = v;

        hold on;
        plot(lambda_M(i,:,j)'*1e9,pow,'color',Color((j-1)+i,:));

    end
end;

%% Data processing

l = lambda_M(1,:,1)'*1e9;
p = pow;
peak_w = zeros(2,1);
peak_v = zeros(2,1);

[pos,v] = peakfinder(p);%, sel);

if ~(isempty(v))
    A = [l(pos)';v'];
    [Y,I]=sort(A(2,:));
    B=A(:,I);

    if length(B(1,:)) > 1
        peak_v(2)=B(2,end-1);
        peak_w(2)=B(1,end-1);
    end
    peak_v(1)=B(2,end);
    peak_w(1)=B(1,end);
end

%% File processing
fname = 'P10';
w_ref = ref_P10;
```

```
fWrite = fopen(strcat(fname,'.txt'),'w');

if length(p) >= length(w_ref(:,1))
    max_len = length(p);
else
    max_len = length(w_ref(:,1));
end

for i=1:max_len
    if i == 1
        % Header
        fprintf(fWrite, 'w, v, w_exp, v_exp, peak1_w, peak1_v, peak2_w,
peak2_v\n');

        fprintf(fWrite, '%6.4f;%6.4f;',l(i), p(i));
        fprintf(fWrite, '%6.4f;%6.4f;',w_ref(i,1),w_ref(i,2));

        fprintf(fWrite,          '%6.4f;%6.4f;%6.4f;%6.4f          \n',
peak_w(1),peak_v(1),peak_w(2),peak_v(2));
    else
        if i<= length(p)
            fprintf(fWrite, '%6.4f;%6.4f;',l(i), p(i));
        else
            fprintf(fWrite, ';;');
        end

        if i<= length(w_ref(:,1))
            fprintf(fWrite, '%6.4f;%6.4f;\n',w_ref(i,1),w_ref(i,2));
        else
            fprintf(fWrite, '\n');
        end
    end
end

hold on;
plot(w_ref(:,1),w_ref(:,2),'b');
axis([1545 1555 -60 0]);


% ======================================
% ======================================
% Runge Kutta Solver  %%%%%%%%%%%%%%%%%%
% ======================================
% ======================================


function R=runge_kutta4_FBG(a, b, N, alpha)

%function runge kutta4() approximates the solution of the IVP
%y' = f(t,y) with t in the interval [a;b] and y(a) = alpha (the initial
condition)
%by the Runge-Kutta method of order four.

%the inputs to this function are:
%a and b: the endpoints of the interval where the solution is to be
approximated
```

```
%N: the number of subdivisions in the interval [a;b]
%alpha: the initial condition
%the ouput is a set of values approximating the solution of the IVP
%some extra lines of code could be added for visualization and
comparison with the exact
%solution if known [plot(t, exact solution as y(t)]

%This file was generated after following a course in numerical methods
at
%the University of Pretoria, Department of Mathematics and Applied
Mathematics
%The algorithmic scheme in this file was drawn from the book of Burden
& Faires
%Numerical Analysis, 7th Ed.

%Author: Alain G. Kapitho
%Date  : Dec. 2005


h = (b-a)/N;            %the step size
z(1) = a;
w(1) = alpha;           %the initial value

for i = 1:N
   k1 = h*f(z(i), w(i));
   k2 = h*f(z(i)+h/2, w(i)+(k1)/2);
   k3 = h*f(z(i)+h/2, w(i)+(k2)/2);
   k4 = h*f(z(i)+h, w(i)+k3);
   w(i+1) = w(i) + (k1 + 2*k2 + 2*k3 + k4)/6;
   z(i+1) = a + i*h;
end

R=[z',w'];

%this line of code below is optional if visualization is not needed

%function relating the right-hand side of the differential equation
%it has to be changed accordingly to the problem at hand
%in this case, the differential equation is: y' = y/t - (y/t)^2

function dy = f(z, y)
global k sigma_h gamma_0 lambda   e_com1 e_com2 dT L alfa DT nu eT
offset;

alfa=0.55e-6;

%apodized Gaussian FBG 2
lambda_D=1550.125e-9;       % nominal
gamma_0=535e-9;             %
n_eff=lambda_D/gamma_0/2;
FWHM=L/3;
a = 1e-5;
b = 5;
del_n_eff=a*exp(-4*log(2)*z^2/FWHM^2);
nu_op=b;
```

```
gamma_s=0*1e-7; %optical chirp
nu=0.17;
p11=0.113;
p12=0.252;
dn_dT=1.241e-5;
pe=n_eff^2/2*(p12-nu*(p11+p12));

de1_dz=0;

if z<=0+offset
    e1=e_com1(1);
    e2=e_com1(2);
    e3=e_com1(3);
else
    e1=e_com2(1);
    e2=e_com2(2);
    e3=e_com2(3);
end

dT=DT;

n_eff_i=-n_eff^3/2*(p12*e2+p12*e1+p11*e3-2/n_eff^3*(dn_dT)*dT-
(p11+2*p12)*alfa*dT)+n_eff;
del_n_eff=del_n_eff*n_eff_i/n_eff;
n_eff=n_eff_i;

gamma=(gamma_0+gamma_s*z)*(1+e1);

dgamma_dz=0; %gamma_s*(1+e1)+(gamma_0+gamma_s*z)*(de1_dz);
phi_prime=0; %2*pi*(-z/gamma^2*dgamma_dz+1/gamma-1/gamma_0);

sigma_h=2*pi*n_eff*1/lambda   -   pi/gamma   +   2*pi*del_n_eff/lambda   -
0.5*phi_prime;

k=pi/lambda*nu_op*del_n_eff;  % K_ac

dy=(-i*k-2*i*sigma_h*y-i*k*y^2);
```

References

[1] E. Udd and W. B. Spillman, *Fiber Optic Sensors: An Introduction to Engineer and Scientists*, 2nd ed. Hooken, NJ: John Wiley & Sons, 2011.

[2] Micron Optics, "Optical Fiber Sensors Guide."

[3] R. Maron, "High sensitivity fiber optic pressure sensor for use in harsh environments," *US Pat. 6,016,702*, 2000.

[4] R. Maron and A. Kersey, "Multi-parameter fiber optic sensor for use in harsh environments," *US Pat. 5,892,860*, 1999.

[5] M. Song, S. B. Lee, S. S. Choi, and B. Lee, "Simultaneous Measurement of Temperature and Strain Using Two Fiber Bragg Gratings Embedded in a Glass Tube," *Opt. Fiber Technol.*, vol. 3, no. 2, pp. 194–196, Apr. 1997.

[6] W. Birch, J. J. den Boer, C. T. M. Doyle, A. Franzen, K. M. Jääskeläinen, and C. B. Staveley, "Pressure sensor assembly and method of using the assembly," US 20110048136 A103-Mar-2011.

[7] J. Yang, Y. Zhao, B.-J. Peng, and X. Wan, "Temperature-compensated high pressure FBG sensor with a bulk-modulus and self-demodulation method," *Sensors Actuators A Phys.*, vol. 118, no. 2, pp. 254–258, Feb. 2005.

[8] M. G. Xu, L. Reekie, J. P. Dakin, and J.-L. Archambault, "Discrimination between strain and temperature effects using dual-wavelength fibre grating sensors," *Electron. Lett.*, vol. 30, no. 13, pp. 1085–1087, Jun. 1994.

[9] G. Brady, K. Kalli, and D. Webb, "Simultaneous measurement of strain and temperature using the first and second-order diffraction wavelengths of Bragg gratings," *Optoelectron. IEE …*, vol. 144, no. 3, 1997.

[10] S. James, M. Dockney, and R. Tatam, "Simultaneous independent temperature and strain measurement using in-fibre Bragg grating sensors," *Electron. Lett.*, vol. 32, no. 12, pp. 1133–1134, 1996.

[11] O. Fraz o, M. J. N. Lima, and J. L. Santos, "Simultaneous measurement of strain and temperature using type I and type IIA fibre Bragg gratings," *J. Opt. A Pure Appl. Opt.*, vol. 5, no. 3, pp. 183–185, May 2003.

[12] X. C. Li, F. Prinz, and J. Seim, "Thermal behavior of a metal embedded fiber Bragg grating sensor," *Smart Mater. Struct.*, vol. 10, no. 4, pp. 575–579, Aug. 2001.

[13] G. R. Fox, C. A. P. Muller, N. Setter, D. M. Costantini, N. H. Ky, and H. G. Limberger, "Wavelength tunable fiber Bragg grating devices based on sputter deposited resistive and piezoelectric coatings," *J. Vac. Sci. Technol. A Vacuum, Surfaces, Film.*, vol. 15, no. 3, p. 1791, May 1997.

[14] A. Iadicicco, S. Campopiano, D. Paladino, A. Cutolo, A. Cusano, and W. Bock, "Gold coated long period gratings in single and multi-layer configuration for sensing applications," vol. 54, pp. 133–136, 2010.

[15] C. Lupi, F. Felli, L. Ippoliti, M. a Caponero, M. Ciotti, V. Nardelli, and a Paolozzi, "Metal coating for enhancing the sensitivity of fibre Bragg grating sensors at cryogenic temperature," *Smart Mater. Struct.*, vol. 14, no. 6, pp. N71–N76, Dec. 2005.

[16] J. A. Jay, "Mechanical Reliability of Optical Fiber," 2011.

[17] Smart Fibres, "FOS Technology Overview," 2013.

[18] J. R. Dunphy, A. D. Hay, R. J. Maron, and P. E. Pruett, "Bourdon tube pressure gauge with integral optical strain sensors for measuring tension or compressive strain." Google Patents, 02-Mar-1999.

[19] BCC Research LLC, "Fiber Optic Sensors: Global Markets," 2011.

[20] Frost and Sullivan, "World Fiber Optic Sensors Markets Report Brochure." [Online]. Available: http://www.frost.com/prod/servlet/report-brochure.pag?id=M633-01-00-00-00. [Accessed: 12-Apr-2014].

[21] Frost and Sullivan, "Fiber Optics Strike a Rich Vein in the Oil and Gas Industry," *Frost and Sullivan*, 2011. [Online]. Available: http://frost.com/sublib/display-press-release.do?id=226808885&bdata=aHR0cHM6Ly9mcm9zdC5jb20vc3JjaC9jYXRhbG9nLXNlYXJjaC5kbz9wYWdlU2l6ZT0xMiZwYWdlPTYwQH5AU2VhcmNoIFJlc3VsdHNAfkAxMzMxMDA1MDkxNjY1. [Accessed: 12-Apr-2014].

[22] "Photonic Sensor Consortium Market Survey Report." [Online]. Available: http://www.igigroup.com/st/pages/photonic_sensor_report.html. [Accessed: 10-Apr-2014].

[23] Corning Incorporated, "Corning SMF-28 Ultra Optical Fiber," 2013. [Online]. Available: http://www.corning.com/WorkArea/showcontent.aspx?id=57651. [Accessed: 01-Apr-2014].

[24] R. Kashyap, *Fiber Bragg Gartings*, 2nd ed. San Diego: Academic Press, 2009, pp. 119–187.

[25] K. O. Hill, Y. Fujii, D. C. Johnson, and B. S. Kawasaki, "Photosensitivity in optical fiber waveguides: Application to reflection filter fabrication," *Appl. Phys. Lett.*, vol. 32, no. 10, p. 647, 1978.

[26] National Aeronautics and Space Administration, "High-Temperature Optical Sensor Allows Testing Up to 1000 ° C," pp. 0–1.

[27] B. Poumellec and P. Niay, "UV-induced densification during Bragg grating writing," *Opt. Mater. 4*, vol. 4, no. March, pp. 441–449, 1995.

[28] T. Erdogan, V. Mizrahi, P. J. Lemaire, and D. Monroe, "Decay of ultraviolet-induced fiber Bragg gratings," *J. Appl. Phys.*, vol. 76, no. 1, p. 73, 1994.

[29] J. Canning, K. Sommer, and M. Englund, "Fibre gratings for high temperature," *Meas. Sci. Technol.*, vol. 12, pp. 824–828, 2001.

[30] J. Archambault, L. Reekie, and P. Russell, "High reflectivity and narrow bandwidth fibre gratings written by single excimer pulse," *Electron. Lett.*, vol. 29, no. 1, pp. 28–29, 1993.

[31] C. G. Askins, M. a Putman, G. M. Williams, and E. J. Friebele, "Stepped-wavelength optical-fiber Bragg grating arrays fabricated in line on a draw tower.," *Opt. Lett.*, vol. 19, no. 2, p. 147, Jan. 1994.

[32] W. Xie, P. Niay, P. Bernage, and M. Douay, "Experimental evidence of two types of photorefractive effects occuring during photoinscriptions of Bragg gratings within germanosilicate fibres," *Opt. …*, vol. 104, pp. 185–195, 1993.

[33] N. Groothoff and J. Canning, "Enhanced type IIA gratings for high-temperature operation.," *Opt. Lett.*, vol. 29, no. 20, pp. 2360–2, Oct. 2004.

[34] M. Fokine, "Underlying mechanisms, applications, and limitations of chemical composition gratings in silica based fibers," *J. Non. Cryst. Solids*, vol. 349, pp. 98–104, Dec. 2004.

[35] J. Canning, "Fiber Bragg grating sensor for high temperature application," *Opto-Electronics Commun. Conf.*, pp. 2006–2007, 2008.

[36] C. M. Jewart, Q. Wang, J. Canning, D. Grobnic, S. J. Mihailov, and K. P. Chen, "Ultrafast femtosecond-laser-induced fiber Bragg gratings in air-hole microstructured fibers for high-temperature pressure sensing.," *Opt. Lett.*, vol. 35, no. 9, pp. 1443–5, May 2010.

[37] D. Grobnic, S. J. Mihailov, C. W. Smelser, and H. Ding, "Sapphire Fiber Bragg Grating Sensor Made Using Femtosecond Laser Radiation for Ultrahigh Temperature Applications," *IEEE Photonics Technol. Lett.*, vol. 16, no. 11, pp. 2505–2507, Nov. 2004.

[38] S. J. Mihailov, "Fiber Bragg grating sensors for harsh environments.," *Sensors (Basel).*, vol. 12, no. 2, pp. 1898–918, Jan. 2012.

[39] J. Echevarria and A. Quintela, "Uniform fiber Bragg grating first-and second-order diffraction wavelength experimental characterization for strain-temperature discrimination," *IEEE Photonics Technol. Lett.*, vol. 13, no. 7, pp. 696–698, 2001.

[40] S. Kreger, S. Calvert, and E. Udd, "High pressure sensing using fiber Bragg gratings written in birefringent side hole fiber," *Opt. Fiber Sensors Conf. Tech. Dig.*, pp. 355–358, 2002.

[41] A. Vengsarkar and W. Michie, "Fiber-optic dual-technique sensor for simultaneous measurement of strain and temperature," *J. Light. Technol.*, vol. 12, no. 1, pp. 170–177, 1994.

[42] W. Urbanczyk, E. Chmielewska, and W. J. Bock, "Measurements of temperature and strain sensitivities of a two-mode Bragg grating imprinted in a bow-tie fibre," *Meas. Sci. Technol.*, vol. 12, no. 7, pp. 800–804, Jul. 2001.

[43] L. Li, J. Geng, L. Zhao, G. Chen, G. Chen, Z. Fang, and C. F. Lam, "Response characteristics of thin-film-heated tunable fiber Bragg gratings," *IEEE Photonics Technol. Lett.*, vol. 15, no. 4, pp. 545–547, Apr. 2003.

[44] A. Ahuja and P. Steinvurzel, "Tunable single phase-shifted and superstructure gratings using microfabricated on-fiber thin film heaters," *Opt. Commun.*, vol. 184, no. October, pp. 119–125, 2000.

[45] B. J. Eggleton, J. a. Rogers, P. S. Westbrook, and T. a. Strasser, "Electrically tunable power efficient dispersion compensating fiber Bragg grating," *IEEE Photonics Technol. Lett.*, vol. 11, no. 7, pp. 854–856, Jul. 1999.

[46] J. a Rogers, B. J. Eggleton, R. J. Jackman, G. R. Kowach, and T. a Strasser, "Dual on-fiber thin-film heaters for fiber gratings with independently adjustable chirp and wavelength.," *Opt. Lett.*, vol. 24, no. 19, pp. 1328–30, Oct. 1999.

[47] Y. Liu, Z. Guo, Y. Zhang, K. Chiang, and X. Dong, "Simultaneous pressure and temperature measurement with polymer-coated fibre Bragg grating," *Electron. Lett.*, 2000.

[48] H. Alemohammad and E. Toyserkani, "Simultaneous measurement of temperature and tensile loading using superstructure FBGs developed by laser direct writing of periodic on-fiber metallic films," *Smart Mater. Struct.*, vol. 18, no. 9, p. 095048, Sep. 2009.

[49] W. T. Zhang, F. Li, Y. L. Liu, and L. H. Liu, "Ultrathin FBG Pressure Sensor With Enhanced Responsivity," *IEEE Photonics Technol. Lett.*, vol. 19, no. 19, pp. 1553–1555, Oct. 2007.

[50] J. Arkwright and S. Doe, "Apparatus for pressure sensing," US 8031988 B22013.

[51] E. J. Jablonski, "Fiber grating package," US 6374014 B116-Apr-2002.

[52] L. Men, P. Lu, and Q. Chen, "A multiplexed fiber Bragg grating sensor for simultaneous salinity and temperature measurement," *J. Appl. Phys.*, vol. 103, no. 5, p. 053107, 2008.

[53] Creganna, "Specialty Needles: Contract Design and Manufacturing," 2011.

[54] Sigma-Aldrich, "Syringe Needle Gauge Chart." [Online]. Available: http://www.sigmaaldrich.com/chemistry/stockroom-reagents/learning-center/technical-library/needle-gauge-chart.html. [Accessed: 12-Apr-2014].

[55] EPO-TEK, "EPO-TEK 353ND Technical Data Sheet," 2014. [Online]. Available: http://www.thorlabs.com/images/tabimages/353nd_290.pdf.

[56] H. R. Alemohammad, E. Foroozmehr, B. S. Cotten, and E. Toyserkani, "A Dual-Parameter Optical Fiber Sensor for Concurrent Strain and Temperature Measurement: Design, Fabrication, Packaging, and Calibration," *Light. Technol. J.*, vol. 31, no. 8, pp. 1198–1204, Apr. 2013.

[57] T. Erdogan, "Fiber Grating Spectra," *Light. Technol. J.*, vol. 15, no. 8, pp. 1277–1294, 1997.

[58] H. Kogelnik, "Theory of Optical Waveguides," *Springer Ser. Electron. Photonics*, vol. 26, pp. 7–88, 1988.

[59] P. C. Autar Kaw, "Runge-Kutta 4th Order Method for Ordinary Differential Equations," in *Ordinary Differential Equations*, 2009, pp. 08.04.1–08.04.07.

[60] H. Alemohammad, "Development of Optical Fiber-Based Sensing Devices Using Laser Microfabrication Methods," University of Waterloo, 2010.

[61] EPO-TEK, "EPO-TEK 353ND-T Technical Data Sheet," 2012. [Online]. Available: http://www.epotek.com/site/administrator/components/com_products/assets/files/Style_Uploads/353ND-T.pdf.

[62] EPO-TEK, "Epoxy Adhesive Application Guide." [Online]. Available: http://www.epotek.com/site/files/brochures/pdfs/adhesive_application_guide.pdf.

[63] AK Steel, "Stainless Steel 304/304L." [Online]. Available: http://www.aksteel.com/pdf/markets_products/stainless/austenitic/304_304l_data_sheet.pdf.

[64] R. Romaniuk, "Tensile strength of tailored optical fibers." Institute of Electronic Systems.

[65] P. Antunes, F. Domingues, M. Granada, and P. André, "Mechanical Properties of Optical Fibers," 2011.

[66] J. F. Nye, *Physical Properties of Crystals: Their Representation by Tensors and Matrices*. Oxford: At the Clarendon Press, 1957.

[67] O. Frazão, L. a. Ferreira, F. M. Araújo, and J. L. Santos, "Applications of Fiber Optic Grating Technology to Multi-Parameter Measurement," *Fiber Integr. Opt.*, vol. 24, no. 3–4, pp. 227–244, May 2005.

[68] A. Omar, "Fiber Optic Sensors: An Introduction for Engineers and Scientists," *Sens. Rev.*, 2013.

[69] Micron Optics, "Optical Sensing Interrogator - sm125 Datasheet."

[70] Parker, "Parker O-Ring Handbook," 2007.

[71] InvarAlloy.com, "Invar Alloy Properties." [Online]. Available: http://www.invaralloy.com/invar-properties.php. [Accessed: 07-Apr-2014].

[72] Swagelok, "Gaugeable Tube Fittings and Adapter Fittings - Data sheet."